A High Conductivity One-Dimensional π-d Conjugated Metal-Organic Framework with Efficient Polysulfide Trapping-Diffusion-Catalysis in Lithium-Sulfur Batteries

Dawei Yang+, Zhifu Liang+, Pengyi Tang+, Chaoqi Zhang, Mingxue Tang, Qizhen Li, Jordi Jacas Biendicho, Junshan Li, Marc Heggen, Rafal E. Dunin-Borkowski, Ming Xu, Jordi Llorca, Jordi Arbiol*, Joan Ramon Morante, Shu-Lei Chou*, Andreu Cabot**

D. W. Yang, Z. F. Liang, C. Q. Zhang, Dr. J. J. Biendicho, Prof. J. R. Morante, Prof. A. Cabot
Catalonia Institute for Energy Research - IREC,
Sant Adrià de Besòs, Barcelona, 08930, Spain
Email: acabot@irec.cat

D. W. Yang, C. Q. Zhang, Prof. J. R. Morante
Department of Electronic and Biomedical Engineering
Universitat de Barcelona, 08028 Barcelona, Spain

Z. F. Liang, Prof. J. Arbiol
Catalan Institute of Nanoscience and Nanotechnology (ICN2)
CSIC and BIST, Campus UAB, Bellaterra, 08193 Barcelona, Spain
Email: arbiol@icrea.cat

Dr. P. Y Tang, Dr. M Heggen, Prof. R E. Dunin-Borkowski
Ernst Ruska-Centre for Microscopy and Spectroscopy with Electrons and Peter Grünberg Institute Forschungszentrum Jü lich GmbH 52425 Jülich, Germany

Dr. P. Y Tang
State Key Laboratory of Information Functional Materials, 2020 X-Lab, ShangHai Institute of Microsystem and Information Technology, Chinese Academy of Sciences, Shanghai, P. R. China

Prof. M. X. Tang
Center for High Pressure Science and Technology Advanced Research, Beijing 100094, China

Q. Z. Li
Department of Biomedical Engineering, Southern University of Science and Technology (SUSTech), Shenzhen, Guangdong, 518055, China

Dr. J. S. Li

Institute of Advanced Study, Chengdu University, Chengdu 610106, China

Prof. J. Llorca
Institute of Energy Technologies, Department of Chemical Engineering and Barcelona Research Center in Multiscale Science and Engineering, Universitat Politècnica de Catalunya, EEBE, 08019, Barcelona, Spain

Prof. M. Xu
State Key Laboratory of Chemical Resource Engineering, Beijing University of Chemical Technology, Beijing 100029, P. R. China
Email: mingxu@mail.buct.edu.cn

Prof. S. L. Chou
Institute for Carbon Neutralization, College of Chemistry and Materials Engineering, Wenzhou University, Wenzhou, Zhejiang 325035, China
E-mail: chou@wzu.edu.cn

Prof. J. Arbiol, Prof. A. Cabot
ICREA
Pg. Lluís Companys 23, 08010 Barcelona, Spain

+ These authors contributed equally to this work

Keywords: metal organic framework, lithium polysulfide, π-d conjugation, lithium-sulfur battery

Abstract

The shuttling behaviour and sluggish conversion kinetics of the intermediate lithium polysulfides (LiPS) represent the main obstructions to the practical application of lithium-sulfur batteries (LSBs). Herein, we present a one-dimensional (1D) π-d conjugated metal-organic framework, Ni-MOF-1D, as an efficient sulfur host to overcome these limitations. Experimental results and density functional theory (DFT) calculations demonstrate that Ni-MOF-1D is characterized by a remarkable binding strength for trapping soluble LiPS species. Ni-MOF-1D also acts as an effective catalyst for S reduction during the discharge process and Li_2S oxidation during the charging process. In addition, the delocalization of electrons in the π-d system of Ni-MOF-1D provides a superior electrical conductivity to improve electron transfer. Thus, cathodes based on Ni-MOF-1D enable LSBs with excellent performance, e.g., impressive cycling stability with over 82% capacity retention over 1000 cycles at 3 C, superior rate performance of 575 mAh g^{-1} at 8 C, and a high areal capacity of 6.63 mAh cm^{-2} under raised sulfur loading of 6.7 mg cm^{-2}. The strategies and advantages here demonstrated can be extended to a broader range of π-d conjugated MOFs materials, which we believe have a high potential as sulfur hosts in LSBs.

1. Introduction

Lithium-sulfur batteries (LSBs) have attracted extensive interest as the next generation of energy storage systems due to the ultra-high theoretical capacity of sulfur (1672 mAh g^{-1}), their high theoretical energy density (2600 W h kg^{-1}), low cost and potential for low environmental impact.[1-3] However, their commercial application is delayed by several unsolved challenges, including: i) the electrically insulating nature of sulfur and its sluggish redox reaction requiring a high polarization; [4,5] ii) the solubility of lithium polysulfides (LiPS) in the liquid electrolyte and its diffusion and deposition on the lithium anode, which lead to a severe capacity decline and a low coulombic efficiency;[6,7] iii) the huge cathode volume change (up to 80%) during operation that may lead to significant structural degradations.[8]

Owing to the enormous potential socio-economic impact of LSBs, intense efforts are being dedicated to solving their limitations. The most extended strategy is to incorporate a high surface area carbonaceous sulfur host on the cathode to provide the required high electrical conductivity, retain LiPS and confine the volume expansion. However, while several carbon-based materials, including graphene, carbon nanotubes and hollow carbon spheres, have been employed as sulfur host in LSB cathodes,[9-12] the physical retention of LiPS by carbon meso-/micropores has limited effectiveness due to the weak van der Waals interaction between the nonpolar surface of carbon and the polar LiPS.[13] To promote this interaction, the incorporation of additional inorganic compounds, e.g. transition-metal oxides,[14] nitrides,[15] and sulfides,[16] with strong dipole-dipole interaction with LiPS, have been proved effective to inhibit the LiPS shuttle effect.[17] As for drawbacks, most of these polar hosts suffer from a relatively poor

electrical conductivity, a moderate density of adsorption sites, and relatively high weight, which result in a poor rate performance and modest specific and gravimetric capacities.[18]

Metal-organic frameworks (MOFs) with a very large density of LiPS adsorption sites have a huge potential as sulfur hosts.[19,20] The Lewis acid-base interactions between MOFs and LiPS have been demonstrated to effectively restrain the migration of LiPS, thus improving the LSB performance.[21,22] Besides, their large structural and chemical diversity provide numerous degrees of freedom to optimize their performance. Nevertheless, most MOFs are electrical insulators. Thus, to be applied as cathode material in LSBs, MOFs are typically combined with additional conductive materials or are carbonized through annealing at high temperatures.[22] Alternatively, π-d conjugated MOFs, which are similar to π-π conjugated organic/polymeric materials, potentially offer low cost, functionalization through molecular design, low volume variation during cycling,[23,24] multiple redox centres, and excellent electrical conductivities and stabilities associated with the delocalization of electrons.[25,26] While similar to π-π conjugated materials, π-d structures constructed by the hybridization of the frontier π orbital of the conjugated ligand and the d-orbital of a transition metal, are far less investigated, particularly as sulfur hosts in LSBs.

In this work, we detail the synthesis of a novel one dimensional (1D) π-d conjugated Ni-based MOF (Ni-MOF-1D). We demonstrate the electrons of the Ni-MOF-1D chains to be delocalized forming a large conjugation system and providing parallel 1D paths for electron conduction and Li^+ diffusion fulfilling the wanted requirements for getting a very large density of adsorption sites. We further investigate the electrochemical behaviour of this material as sulfur host in

LSBs and demonstrate that S@Ni-MOF-1D electrodes deliver a superior rate performance and extraordinary stability. The obtained results are rationalized with the help of density functional theory (DFT) calculations.

2. Results and discussions

Ni-MOF-1D complexes were synthesized by coordinating Ni^{2+} with 1,2,4,5-benzenetetramine tetrahydrochloride and the posterior Schiff-based reaction with 1,1,3,3-tetramethoxypropane.[27] In the final product, each Ni^{2+} is coordinated to four N atoms of two 1,2,4,5-benzenetetramine tetrahydrochloride molecules via d-π hybridization (**Figure 1a**). Compared with conventional MOFs, the π-d hybridization within Ni-MOF-1D delivers a large density of delocalized electrons that provides a distinctive high electrical conductivity, exceeding even that of activated carbon.[26,28]

Scanning electron microscopy (SEM) analysis showed the Ni-MOF-1D complexes to form microscopic particles with an irregular morphology (Figure 1b, Figure S1a,b). Energy-dispersive X-ray spectroscopy (EDX) displayed the atomic ratio of Ni and N to be *ca.* 1:4, consistent with the Ni^{2+} bonding to 1,2,4,5-benzenetetramine tetrahydrochloride via its coordination with four N atoms. Aberration-corrected high angle annular dark-field scanning transmission electron microscopy (HAADF-STEM) images coupled with EDX elemental maps (Figure 1c, S1c) showed C, N, and Ni to be homogenously distributed within Ni-MOF-1D. The presence of oxygen was associated with the solvent used for TEM sample preparation, and with the high affinity of Ni-MOF-1D for trapping oxygen and moisture.[29] X-ray diffraction (XRD) analysis showed the Ni-MOF-1D to present a low crystallinity. Besides, XRD patterns displayed no diffraction peak corresponding to a nickel-based crystal structure, which suggested the absence of Ni-related crystalline nanoparticles or clusters (Figure S1d) and is consistent with HAADF-STEM analysis (Figure S2).

Integrated differential phase-contrast STEM (iDPC-STEM) images at different magnifications showed the Ni-MOF structures to have a 1D morphology and to be randomly orientated within the microscopic particles (Figure 1d-f, S3). Taking advantage of the sensitivity of iDPC-STEM to the atomic number, higher magnification images showed Ni, with a higher atomic number than C and N and thus a brighter contrast, to be distributed as single atoms within Ni-MOF (Figure 1g).

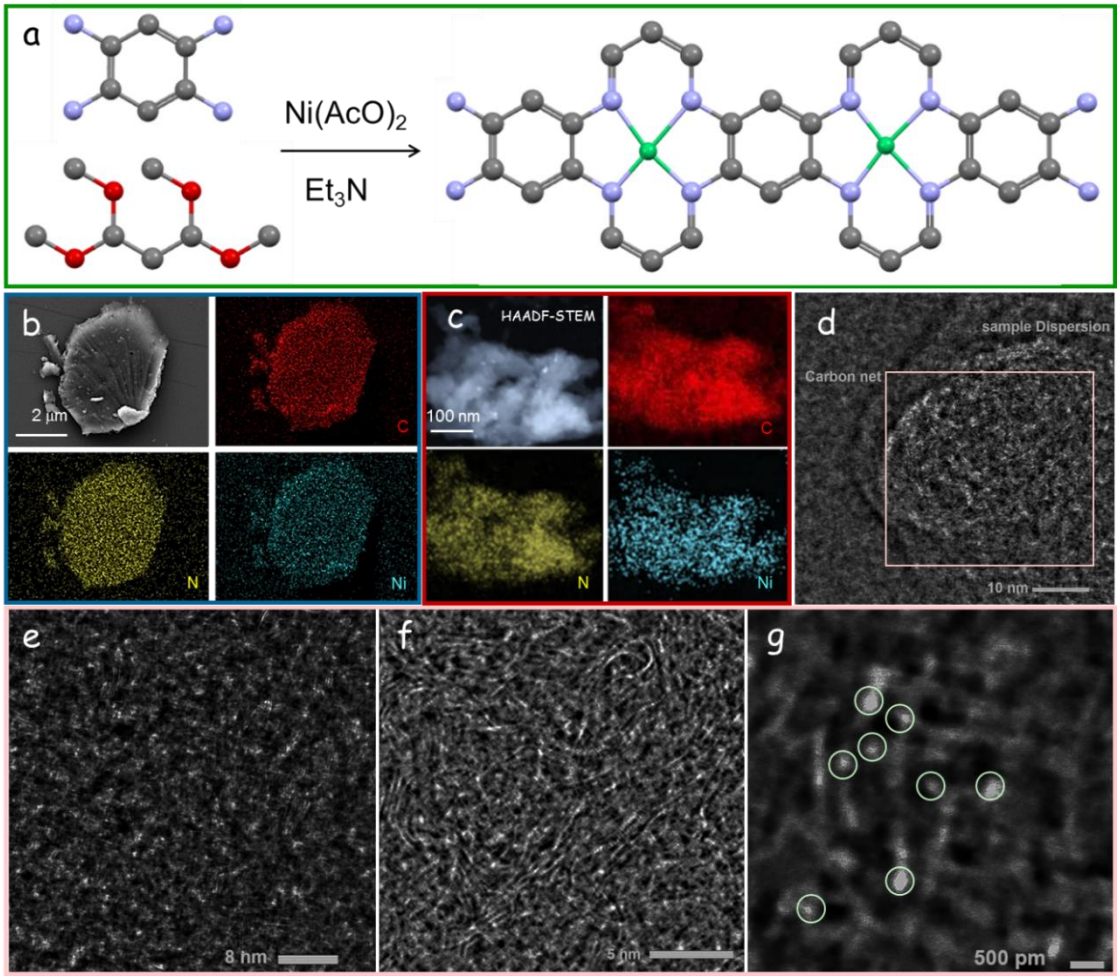

Figure 1. (a) Schematic illustration of the synthesis of Ni-MOF-1D (blue = nitrogen, grey = carbon, red = oxygen, green = nickel). (b) SEM image and SEM-EDX elemental maps of Ni-MOF-1D. (c) STEM-HAADF image and detailed STEM-EDX elemental maps of Ni-MOF-1D. (d-g) iDPC-STEM images at different magnifications of Ni-MOF-1D. Green circles display single Ni atoms shown as bright contrast spots.

X-ray photoelectron spectroscopy (XPS) was used to further analyze the elemental composition and chemical states of Ni-MOF-1D (Figure S4). The high-resolution C 1s XPS spectrum was fitted using four bands, being the main one associated with the C-C bond and used as a reference at 284.6 eV (Figure S4b).[30] The high-resolution N 1s XPS spectrum was fitted with three bands at 398.5 eV, 400.1 eV and 401.5 eV, which correspond to C=N, C-N, H-N bonds, respectively (Figure S4c).[31,32] In the high-resolution Ni 2p XPS spectrum (Figure S4d), a doublet at 855.6 eV (Ni $2p_{3/2}$) and 873.3 eV (Ni $2p_{1/2}$) was assigned to a Ni^{x+} chemical environment.[31,33]

The chemical structure of Ni-MOF-1D and particularly the valence state of Ni was more precisely investigated using X-ray absorption near-edge structure (XANES) measurements using Ni foil and NiO as references (Table S1). As shown in **Figure 2a**, the edge structure of Ni-MOF-1D in the XANES spectra is much closer to that of NiO than to Ni, meaning that the valence state of Ni in Ni-MOF-1D is higher than that of the metallic state, consistently with XPS results.[34,35] The absorption edge position of Ni-MOF-1D was consistent with a Ni coordination environment resembling that of the Ni-N bond in Ni-MOF-1D. The Fourier transformed extended X-ray absorption fine structure (FT-EXAFS) spectrum of the Ni foil displayed a main peak at 2.23 Å standing for the Ni-Ni bond. For NiO, FT-EXAFS peaks at 1.62 Å and 2.69 Å are associated with Ni-O and Ni-Ni bonds, respectively (Figure 2b).[35,36] The FT-EXAFS spectrum of Ni-MOF-1D displayed a peak at 1.40 Å, which was attributed to a Ni-N bond, further demonstrating the coordination of nickel with nitrogen in Ni-MOF-1D.[37] Figure 2c shows the oscillation curves of Ni-MOF-1D, the Ni foil and NiO in the k range 0-

14.0 $Å^{-1}$. Ni-MOF-1D displayed the strongest decrease in signal intensity, pointing towards a higher disorder.

To visualize the coordination environments in both the K and R spaces, a wavelet transform (WT) analysis of the Ni k-edge EXAFS spectrum was carried out (Figure 2d-f, S5). The contour plot of the reference Ni foil exhibited a WT maximum at 7.2 $Å^{-1}$, associated with Ni-Ni. The reference NiO exhibited two WT maxima, at 6.8 $Å^{-1}$ and 5.0 $Å^{-1}$, corresponding to Ni-Ni and Ni-O, respectively. Ni-MOF-1D displayed a single WT maximum located at 4.6 $Å^{-1}$, consistent with the Ni-N chemical environment.[36]

The ^{1}H magic angle spinning nuclear magnetic resonance (MAS-NMR) spectrum of Ni-MOF-1D extended to 160 ppm accounting for all the spinning sidebands (SSBs) due to the rigid character of the molecule (Figure S6). To determine the isotropic signal, spectra were acquired at MAS speeds of 8 kHz and 10 kHz. The SSBs vary position upon changing spinning rate, while the isotropic peak remains the same. For better clarity, only the isotropic ^{1}H NMR signal and its simulation are displayed in Figure 2g. The two resonances appearing at -1.1 and -1.3 ppm are assigned to the protons attached to the N/Ni hybrid hexatomic ring and the ones bonded to the aromatic ring in the main chain, respectively. Additionally, the occupancies of the two sorts of protons are 73% and 27%, consistently with the structure. The negative ^{1}H shifts are mainly attributed to the shielding from the synergistic effect of Ni atoms and the electron cloudy distribution in space.[38,39] Moreover, the broad unresolved ^{13}C NMR spectrum, as displayed in Figure 2h, also confirms the hard structure of the material. The central resonances in the range 120 - 160 ppm arise from the aromatic carbons and C=C in the hybrid rings.

Fourier transform infrared spectroscopy (FT-IR) was performed to evaluate the formation of Ni 1D-MOF (Figure 2i). The peak at 1582 cm^{-1} is a fingerprint of Ni(II) coordinated with C=N, suggesting the coordination structure of Ni(II) tetraaza[14]annulenes as we proposed.[27] The peak at 1618 cm^{-1} is assigned to the deformation vibration of NH_2, suggesting the existence of NH_2 at the edge of Ni-MOF-1D.

The presence of delocalized electrons was further confirmed by continuous-wave electron paramagnetic resonance (CW-EPR) analysis. Ni-MOF-1D displays a narrow and weak EPR resonance at 320 mT which cannot be assigned to Ni but to the delocalized electrons along its double bond (Figure 2j).[40,41]

The electronic band structure of Ni-MOF-1D obtained from the DFT calculations within the HSE06 functional and the corresponding first Brillouin zone are displayed in Figure 2k,l. Several bands cross the Fermi level, demonstrating the metallic nature of Ni-MOF-1D.[26,31]

Figure 2m shows the charge density projected-real space for Ni-MOF-1D. The charge density projections to the x-axis and y-axis directions are presented in Figure S7. A positive charge density expands along the y-axis direction, i.e. along the Ni-MOF-1D extending direction. On the other hand, on the x-axis, the charge density is zero outside of the range 4-13 Å. Thus, the charge is more easily transferred along the y-axis than the x-axis.

The electron localization function (ELF) was used to investigate the covalence/iconicity of Ni-MOF-1D (Figure 2n and S8).[42,43] The warmer the colour, ELF values closer to 1, the fewer the delocalized electrons, and the weaker the catalytic ability to regulate the adsorbed species. It

can be seen that there are delocalized electrons around Ni, which can efficiently regulate the adsorbent, pointing at the Ni centre as the catalytic active site.

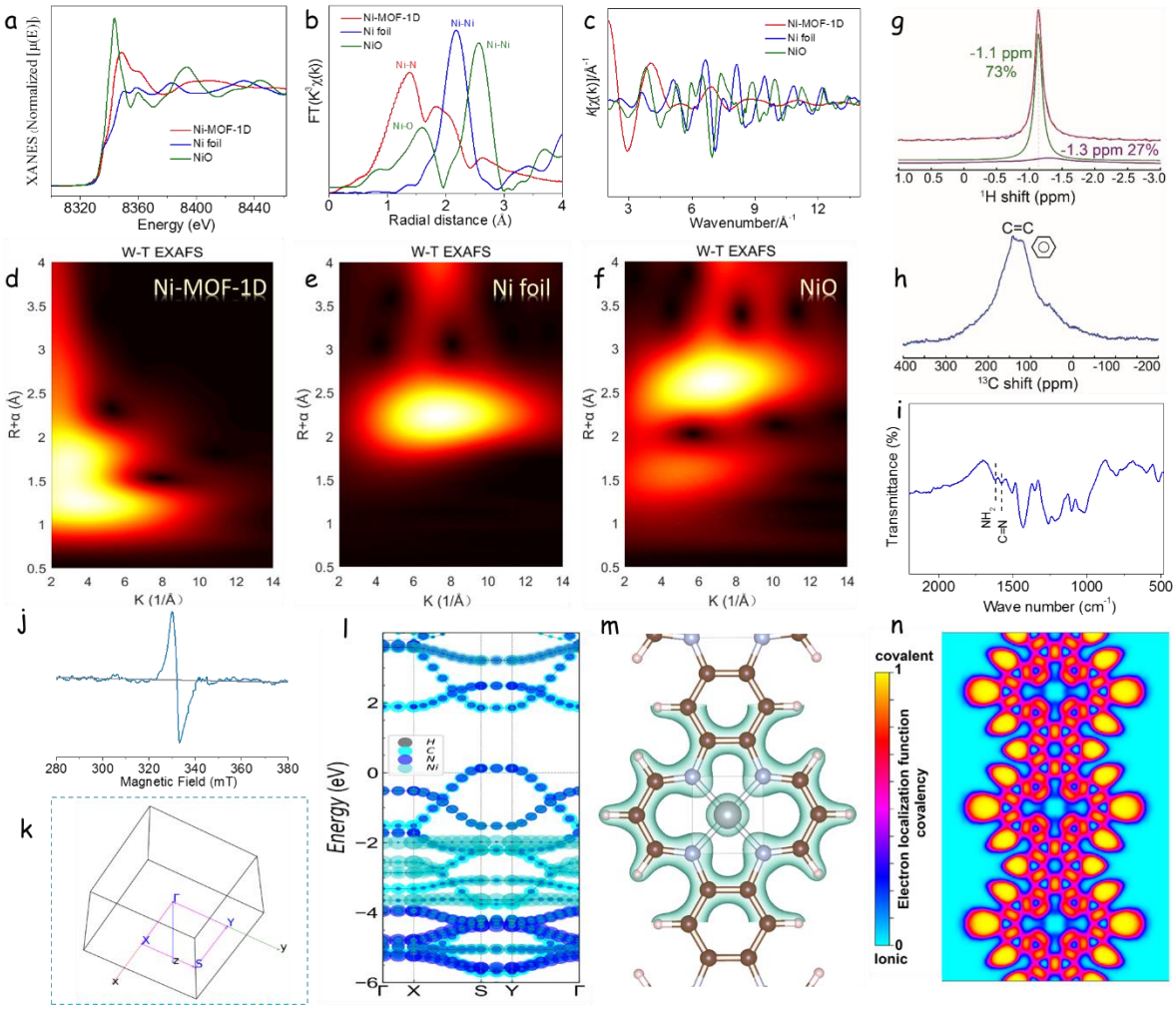

Figure 2. (a) XANES spectra of Ni-MOF-1D, a Ni foil and NiO. (b) Ni K-edge FT-EXAFS spectra in R space of Ni-MOF-1D, Ni foil and NiO.. (c) EXAFS oscillations of Ni-MOF-1D with respect to the reference samples. (d-f) Wavelet transform contour plots at Ni K-edge of Ni-MOF-1D, Ni foil, and NiO. (g) Isotropic signal of ^{1}H NMR spectrum and (h) ^{13}C MAS-NMR spectrum for Ni-MOF-1D. In (g), the blue curve displays the experimental data and the red-dashed line is the simulation. The position and occupancy are marked next to each resonance. (i) FTIR spectra of Ni-MOF-1D sample. (j) CW-EPR spectrum of Ni-MOF-1D, with g factor of 1.998, being a footprint of delocalized electrons within the polymer. (k) First Brillouin zone, (l) calculated electronic band structure, (m) charge density, and (n) ELF of Ni-MOF-1D.

To evaluate the performance of Ni-MOF-1D as sulfur host in LSBs, sulfur was introduced within the Ni-MOF-1D through a melt infiltration process. SEM-EDX elemental maps displayed the four elements, S, C, N, and Ni, to be uniformly distributed throughout the composite material (Figure S9a,b). The XRD pattern of S@Ni-MOF-1D further confirmed the loading of crystalline sulfur (JCPDS No. 65-1101) within S@Ni-MOF-1D composite (Figure S9c).[44] Thermogravimetric analysis (TGA) quantified the sulfur content in the S@Ni-MOF-1D composite at 70.2 wt% (Figure S9d). Besides, the Brunauer–Emmett–Teller (BET) specific surface area of Ni-MOF-1D was 216.8 $m^2 g^{-1}$, and it decreased to 8.6 $m^2 g^{-1}$ with the loading of the porous structure with sulfur (Figure S9e). These results overall illustrate the successful incorporation of sulfur into Ni-MOF-1D.

The four-point probe method was used to determine the electrical conductivities of the host materials before and after sulfur fusion (Figure S10). Ni-MOF-1D exhibited a relatively high electrical conductivity of 156.7 S cm^{-1}, more than one order of magnitude above that of a porous carbon reference (Super P, 12.5 S cm^{-1}). After fusion with sulfur, S@Ni-MOF-1D showed an electrical conductivity up to 19.1 S cm^{-1}, nearly fivefold above that of S@Super P (3.8 S cm^{-1}). To study the LiPS adsorption ability of the host material, the same amounts of Ni-MOF-1D and the Super P carbon reference were immersed in a 1×10^{-2} M Li_2S_4 solution. After 12h, the solution containing Super P still displayed the dark yellow colour of the initial Li_2S_4 solution, while the solution containing Ni-MOF-1D was mostly transparent. This observation was confirmed by the UV–vis spectrum of the solution in the range of 400-500 cm^{-1} (**Figure 3a**). Ni-MOF-1D showed the lowest LiPS-related absorbance peaks, indicating the least amount of

LiPS residue in the solution. This result demonstrates the strong LiPS adsorption capability of Ni-MOF-1D compared with a conventional carbonaceous support.[45,46]

The high-resolution N 1s and Ni 2p XPS spectra obtained from Ni-MOF-1D before and after Li_2S_4 adsorption are displayed in Figures 3b and 3c, respectively. After the Li_2S_4 adsorption, the Ni 2p and N 1s peaks showed a significant shift to higher binding energies, which denoted a strong chemical interaction between Li_2S_4 and Ni-MOF-1D.[29]

To further evaluate the interaction between LiPS and Ni-MOF-1D, DFT calculations were conducted. Figures S11 and S12 display the optimized adsorption configuration of LiPS species at six different lithiation stages (Li_2S, Li_2S_2, Li_2S_4, Li_2S_6, Li_2S_8 and S_8) on Super P and Ni-MOF-1D. The strong interaction between LiPS species and Ni-MOF-1D is related to a Lewis acid-base interaction. The electrons of polysulfide anions can be transferred to the unfilled d orbitals of the Ni sites on Ni-MOF-1D, forming a Ni-S bonding. Besides, the Li Lewis acids in LiPS species having unoccupied orbitals can form chemical bonds with the N Lewis base in Ni-MOF-1D, having lone electron pairs.[21,46] Taking Li_2S_4-adsorbed structures as an example (Figure 3d), a binding energy (E_b) of -4.59 eV on Ni-MOF-1D was calculated. Figure 3e further displays the E_b of LiPS species at six different lithiation stages. DFT calculations showed the absolute binding energies for Ni-MOF-1D to be higher than those for the porous carbon used as a reference, Super P. These results suggest robust chemisorption of LiPS species on Ni-MOF-1D, demonstrating its high potential effectiveness to suppress the LiPS shuttle effect.

DFT calculations were further conducted to uncover the redox kinetics of the LiPS conversion. The initial state, transition state and final state of Li_2S decomposition on Ni-MOF-1D and

carbon are displayed in Figures S13 and S14. As shown in Figure 3f, the calculated decomposition energy barrier of Li_2S on the surface of the Ni-MOF-1D was just 0.67 eV that was much lower than carbon (2.12 eV). Thus, Ni-MOF-1D could greatly reduce the Li_2S decomposition energy barrier, facilitate delithiation reaction kinetics and enhance the redox reversibility between Li_2S and LiPS in the electrochemical process.[36,47]

Besides, the Gibbs free energies for the S reduction pathways of Ni-MOF-1D cathodes were calculated. The overall process of the reversible formation of Li_2S from S_8 and Li was considered. During the discharge process, the first step involves the double reduction of S_8 with two Li^+ to form Li_2S_8, and then Li_2S_8 undergoes further reduction, forming three intermediate LiPS; Li_2S_6, Li_2S_4, and Li_2S_2, producing Li_2S as the final product. The optimized configuration of the intermediates and their Gibbs free energy profiles is shown in Figure 3g. The largest increase of Gibbs free energy was obtained for the conversion from Li_2S_2 to Li_2S species, suggesting this step as the rate-limiting for the total discharge process.[29,47] The free energy increase was lower for Ni-MOF-1D (0.75 eV) than for carbon (1.17 eV), suggesting that the reduction of S is more thermodynamically favourable on Ni-MOF-1D than on carbon substrate.

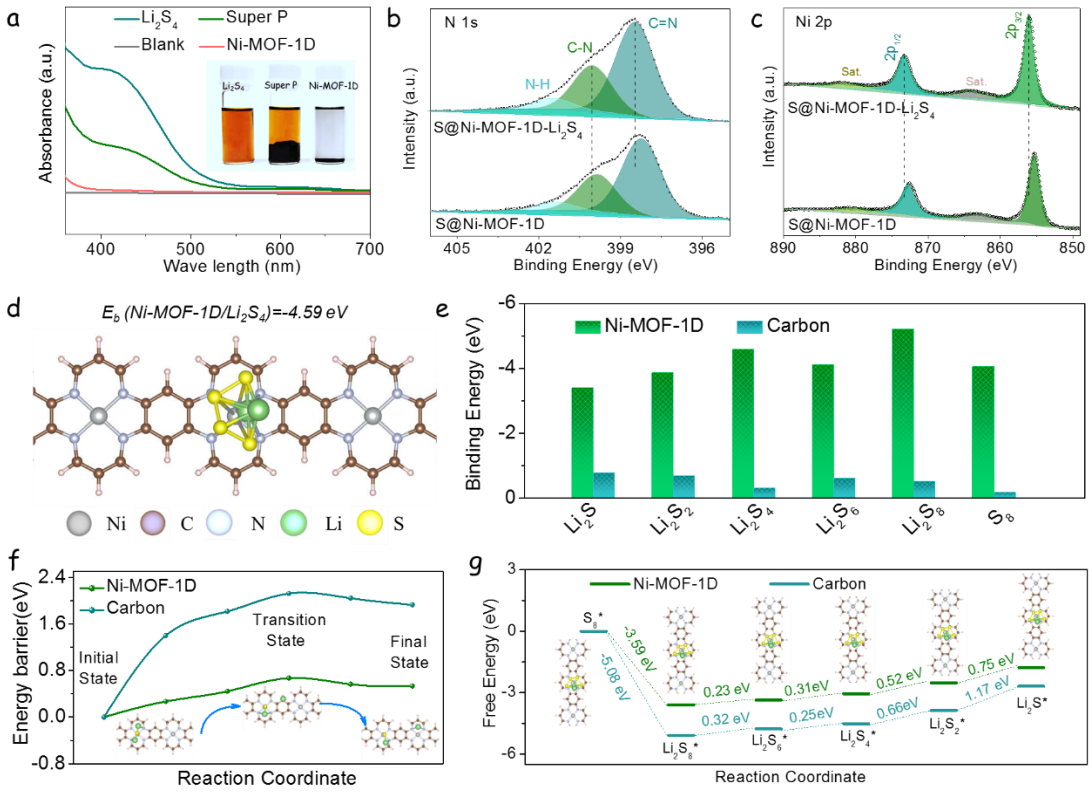

Figure 3. (a) UV−Vis spectra and optical images of the polysulfide solutions after interaction with different adsorbents overnight. (b) High-resolution N 1s XPS spectra from Ni-MOF-1D before and after the Li_2S_4 adsorption test. (c) High-resolution Ni 2p XPS spectra of Ni-MOF-1D before and after adsorption of Li_2S_4. (d) Relaxed Li_2S_4-adsorbed structure on the surface of Ni-MOF-1D calculated with DFT. (e) Binding energies between LiPS species (Li_2S, Li_2S_2, Li_2S_4, Li_2S_6, Li_2S_8 and S_8) and Ni-MOF-1D or carbon as calculated by DFT. (f) Decomposition energy barriers of Li_2S on Ni-MOF-1D and carbon for different adsorbate configurations. (g) Gibbs free energy profiles and adsorption conformation of LiPS species on Ni-MOF-1D, showing a much lower reaction free energy from Li_2S_2 to Li_2S on Ni-MOF-1D than carbon.

To analyze the electrocatalytic activity of Ni-MOF-1D for polysulfide conversion, CV measurements on a symmetric cell were performed within a voltage window of -1.0 to 1.0 V in a 0.5 M Li_2S_6 and 1 M LiTFSI DOL/DME (v/v = 1/1) electrolyte (**Figure 4a**). Ni-MOF-1D

electrodes exhibited a cathodic peak at -0.30 V and an anodic peak at 0.30 V associated with the reaction:[48]

$$S_6^{2-} + 10e^- + 12Li^+ \leftrightarrow 6Li_2S \quad (1)$$

and another cathodic peak at -0.25 V and anodic peak at 0.25 V that correspond to the reaction:

$$4S_6^{2-} \leftrightarrow 8e^- + 3S_8 \quad (2)$$

CV curves of symmetric cells with Ni-MOF-1D electrodes displayed significantly higher peak current densities than cells with Super P electrodes. These results demonstrate that Ni-MOF-1D electrodes accelerate the electrochemical reduction and oxidation reaction kinetics of liquid-to-solid ($Li_2S \leftrightarrow S_6^{2-} \leftrightarrow S_8$) conversion. Besides, approximately rectangular-shaped CV curves were obtained from Ni-MOF-1D electrodes in a Li_2S_6-free electrolyte, suggesting a pure capacitive behaviour (Figure S15a).[46,49]

Almost unchanged CV curves were obtained during 50 cycles, pointing toward an excellent stability of the Ni-MOF-1D electrodes (Figure S15b). A similar CV profile was also obtained at different scanning rates from symmetric cells with Ni-MOF-1D electrodes (Figure S15c). Figure S16 shows the electrochemical impedance spectroscopy (EIS) results obtained from Ni-MOF-1D and Super P electrodes, and the simulated equivalent circuit. EIS data shows the Ni-MOF-1D electrodes to be characterized by much lower charge-transfer resistance (R_{ct}) than Super P, which points at a significantly faster charge transfer at the Ni-MOF-1D/polysulfide interface than at the Super P/polysulfide interface.[46]

CV measurements using LSB coin cells based on S@Ni-MOF-1D and S@Super P cathodes are presented in Figure 4b. A first cathodic peak (peak I) was identified with the reactions:[50,51]

$$S_8 + 2e^- + 2Li^+ \rightarrow Li_2S_8$$

$$3Li_2S_8 + 2e^- + 2Li^+ \rightarrow 4Li_2S_6$$

$$2Li_2S_6 + 2e^- + 2Li^+ \rightarrow 3Li_2S_4$$

The second cathodic peak (peak II) accounted for the reactions:

$$Li_2S_4 + 2e^- + 2Li^+ \rightarrow 2Li_2S_2$$

$$Li_2S_2 + 2e^- + 2Li^+ \rightarrow 2Li_2S$$

The anodic peak (peak III) corresponded to the reverse oxidation of short-chain sulfides to LiPS and eventually to sulfur.[52] S@Ni-MOF-1D electrodes displayed much higher peak currents and more positive/negative potentials of the cathodic/anodic peaks than S@Super P, demonstrating the effective role of Ni-MOF-1Din promoting the LiPS catalytic redox reaction (Figure 4b,c). The catalytic activity was quantified through the onset potential at 10 μA cm^{-2} beyond the baseline current (Figure S17, 4c).[29,53] The cells based on S@Ni-MOF-1D electrodes systematically showed higher onset potentials of cathodic peaks (peak I and peak II) and lower onset potentials of the anodic peak (peak III) with respect to cells based on S@Super P, demonstrating faster kinetics of the LiPS redox reaction.

The electrocatalytic activity of Ni-MOF-1D-based electrodes was further analyzed by CV at different scan rates, from 0.1 to 0.5 mV s^{-1} (Figure 4d). When increasing the scan rate, S@Ni-MOF-1D-based cells exhibited higher redox peak currents and lower polarization potentials compared with S@Super P-based cells (Figure S18). Besides, the CV curves measured from S@Ni-MOF-1D cathodes almost overlap during the first four cycles, demonstrating good reversibility of the sulfur redox reactions (Figure S19). The cathodic and anodic peak currents

(I, II, III and IV) showed a linear relationship with the square root of the scanning rate, consistently with a diffusion-limited reaction. Thus, the diffusion constant of lithium ions (D_{Li+}) was calculated through the classical Randles–Sevcik equation:[54,55]

$$I_p = (2.69*10^5)n^{1.5}AD_{Li^+}{}^{0.5}C_{Li^+}v^{0.5}$$

Where I_p is the peak current density, n is the electron transferred number, A is the geometric area of the electrode, C_{Li+} is the concentration of Li^+ in the electrolyte, and v is the scan rate. A, n, and C_{Li+} are constant in this equation, thus sharper $I_p/v^{0.5}$ slopes denote faster Li^+ diffusion. As displayed in Figure S20, compared with S@Super P, S@Ni-MOF-1D electrodes exhibited the sharpest slopes, pointing towards the highest Li^+ diffusivity during the redox reactions. In peak I, II, III and IV, S@Ni-MOF-1D electrodes were characterized by a D_{Li+} of 2.0×10^{-7}, 3.2×10^{-7}, 5.2×10^{-7}, and 6.1×10^{-7} cm^2 s^{-1}, respectively, significantly above those of S@Super P (Figure 4e). We assigned the higher Li^+ diffusivities to the relief of the shuttle effect and the outstanding catalytic activity of the Ni-MOF-1D host in accelerating the LiPS conversion kinetics. These properties contributed to preventing the formation of a high viscosity electrolyte through the dissolution of LiPS and the deposition of insulating Li_2S_2/Li_2S on the electrode.[49,54]

The galvanostatic charge/discharge profiles for S@Ni-MOF-1D and S@Super P electrodes at a current rate of 0.1 C are displayed in Figure 4f. The charge/discharge curves displayed two discharge plateaus and one charge plateau, which is consistent with CV results and to the multistep sulfur reaction mechanism. The voltage gap between the second discharge and the charge plateaus was considered as the polarization potential (ΔE).[46,56] S@Ni-MOF-1D

electrodes displayed a lower polarization potential (ΔE = 131 mV) than S@Super P electrodes (ΔE = 208 mV) (Figure 4g), again consistent with the superior catalytic activity of Ni-MOF-1D to accelerate the conversion of LiPS.

Another quantitative indication of the catalytic activity of the host materials toward the LiPS conversion reaction is the ratio Q2/Q1, where Q1 is the capacity of the first discharge plateau ascribed to the reduction of sulfur to soluble LiPS ($S_8 + 4Li^+ + 4e^- \rightarrow 2Li_2S_4$), and Q2 is the capacity of the second discharge plateaus, corresponding to the subsequent reduction to insoluble sulfide ($2Li_2S_4 + 12Li^+ + 12e^- \rightarrow 8Li_2S$).[57,58] If all soluble LiPS are further reduced to insoluble lithium sulfide, Q2/Q1=3. Thus, host materials with high catalytic activity toward LiPS reduction provide Q2/Q1 ratios close to 3. S@Ni-MOD-1D exhibited an excellent Q2/Q1 = 2.80, well above that of the porous carbon host (S@Super P, Q2/Q1=1.79, Figure 4g).

S@Ni-MOF-1D electrodes also involved a lower overpotential than S@Super P for LiPS reduction to Li_2S_2/Li_2S and Li_2S oxidation, as observed in the smaller voltage step at the initial discharging period (Figure 4h),[47] and the smaller voltage dip at the beginning of the initial charging period (Figure S21),[54] respectively.

Potentiostatic nucleation and dissolution experiments were performed to further assess the catalytic effect of the electrode materials on the reversible reaction between polysulfides and Li_2S_2/Li_2S. As shown from the potentiostatic discharge profiles in Figure 4i, Ni-MOF-1D electrodes exhibit shorter nucleation and growth times, and higher capacity of Li_2S precipitation (303.5 mA h g^{-1}) than Super P electrodes (115.6 mA h g^{-1}), as calculated based on Faraday's

law. This result further suggests that Ni-MOF-1D significantly lowers the energy barrier of the Li_2S nucleation, accelerating the Li_2S precipitation kinetics.[49,59]

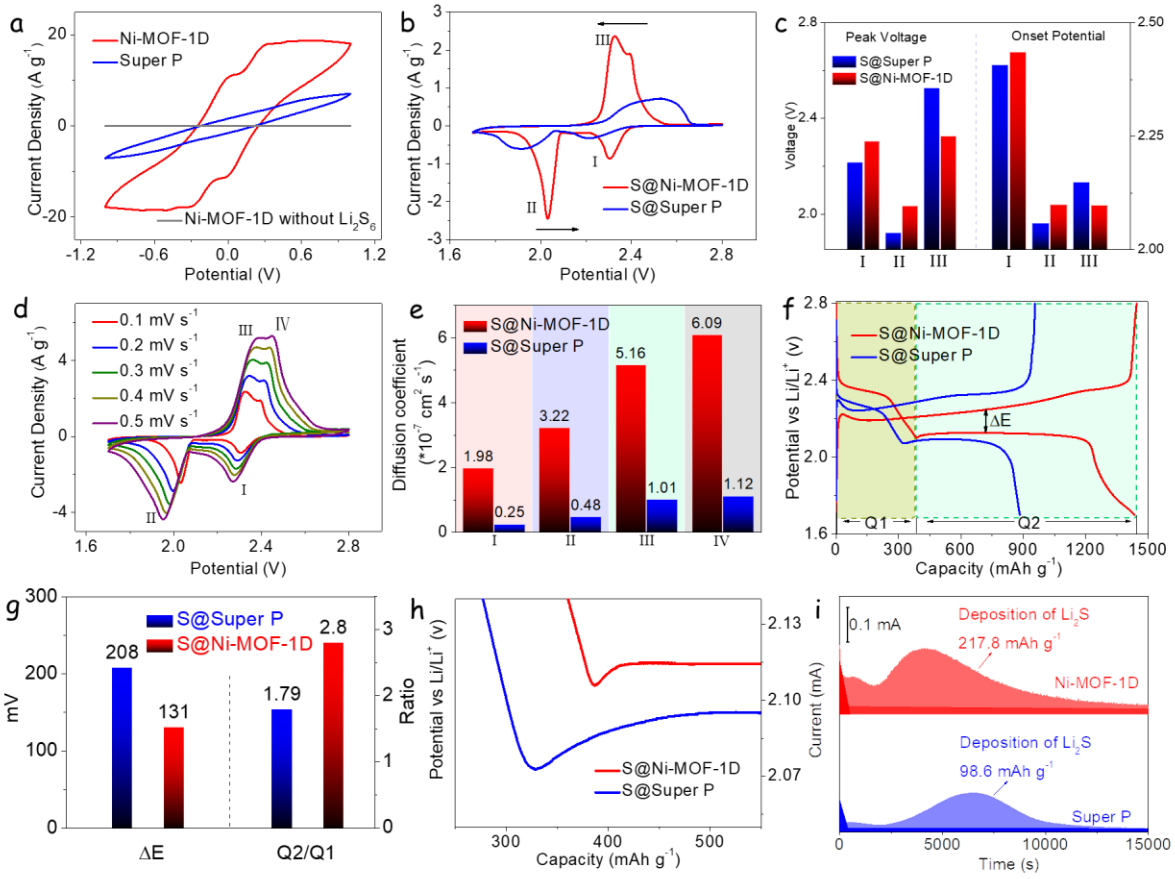

Figure 4. (a) CV profiles of symmetric cells with Ni-MOF-1D and Super P host materials in an electrolyte containing 0.5 mol L^{-1} Li_2S_6 and 1 mol L^{-1} LiTFSI dissolved in DOL/DME (v/v = 1/1). (b) CV profiles of Li-S coin cells at a scan rate of 0.1 mV s^{-1}. (c) Peak voltages and onset potentials of Li-S cells based on the CV curves. (d) CV profile of the S@Ni-MOF-1D electrode with scan rates ranging from 0.1-0.5 mV s^{-1}. (e) Li^+ diffusion coefficient of S@Ni-MOF-1D and S@Super P electrodes calculated from I, II, and III. (f) Galvanostatic charge/discharge profiles of various electrodes with a 0.1 C current rate. (g) Values of ΔE and Q2/Q1 obtained from charge/discharge profiles. (h) Discharge curves of S@Ni-MOF-1D and S@Super P electrodes exhibiting the overpotentials for the transformation from soluble LiPS to insoluble

Li_2S_2/Li_2S. (i) Potentiostatic discharge profile at 2.05 V on S@Ni-MOF-1D and S@Super P electrodes with Li_2S_8 catholyte to evaluate the nucleation kinetics of Li_2S.

Figure 5a presents the galvanostatic charge/discharge profiles of S@Ni-MOF-1D at different current rates. All discharge curves display two well-defined plateaus, even at the highest current density tested, 8 C. In contrast, S@Super P electrodes showed a high polarization potential and no capacity response at current rates above 3 C (Figure S22a), due to the large potential barriers and limited conductivity that characterize this electrode material. Figure 5b displays the rate performances of different cells at current rates from 0.1 to 8 C. S@Ni-MOF-1D exhibited a very high initial discharge capacity of 1491 mA h g^{-1} at 0.1 C, demonstrating an optimized activity and usage of sulfur. Even at 8 C, the average capacity stabilized at 575 mAh g^{-1}. When switched back to 0.2 C, the capacity obtained from the S@Ni-MOF-1D electrode returned to approximately 1150 mAh g^{-1}, corresponding to 95.8% of its initial value, pointing toward remarkable reversibility and stability.

The energy conversion efficiency of LSBs in the charging/discharging process was calculated by the ratio of energy output/input:[53,60]

$$E = \int UIdt$$

As shown in Figure 5c, S@Ni-MOF-1D electrodes were characterized by higher energy efficiencies, around 93.0% at 0.1 C than S@Super P (90.8%). Differences in energy efficiency became more notorious when increasing the current rate. At 3C, S@Ni-MOF-1D stabilized the energy efficiency at 87.2%, well above that of S@Super P electrodes (71.3%). We associate these higher energy efficiencies with the lower polarization potentials and better catalytic activity of Ni-MOF-1D.

To evaluate the cycling stability of different host materials, cells based on S@Ni-MOF-1D and S@Super P cathodes were galvanostatically cycled at 1 C (Figure 5d). S@Ni-MOF-1D electrodes enabled an initial capacity of 913 mAh g^{-1}, and retained about 94.8% capacity, 869 mAh g^{-1}, after 200 cycles. In contrast, S@Super P electrodes displayed a discharge capacity of 408 mAh g^{-1} with a capacity retention of 58.3% after 200 cycles. These notable differences might be attributed to the more effective LiPS management and the suppressed shuttle effect achieved by Ni-MOF-1D.

Figure 5e shows the Nyquist plot of the EIS data obtained from S@Ni-MOF-1D coin cells before and after cycling at 1 C. The fitting of the data showed S@Ni-MOF-1D electrodes to be characterized by much lower R_{ct} compared with S@Super P (Figure S22b), indicating improved electrode kinetics.[61]

Long-cycling tests out of cells based on S@Ni-MOF-1D electrodes were carried out at a higher current rate of 3 C (Figure 5f). After 1000 cycles at 3 C, S@Ni-MOF-1D electrodes still delivered a discharge capacity of 588 mAh g^{-1} with an average 0.018% decay per cycle and a stable and high coulombic efficiency above 99.6%.

Increasing the sulfur loading and decreasing the electrolyte addition are mandatory to achieve the high energy density LSBs required in practical applications.[62,63] Hence, Figure 5g investigates the high-loading performance of the S@Ni-MOF-1D electrodes at the sulfur loading of 4.3, 5.5, and 6.7 mg cm^{-2} at 0.1 C, corresponding to the electrolyte-to-sulfur (E/S) ratio of 12.0, 9.4, and 7.6 µL mg^{-1}, respectively. The S@Ni-MOF-1D enables a high areal capacity of 6.63 mAh cm^{-2} under the raised sulfur loading up to 6.7 mg cm^{-2}. The long-term

performance was tested under a higher loading of 7.6 mg cm^{-2} with a lean electrolyte condition (E/S < 5µL mg^{-1}) at 0.5 C (Figure S23). After 110 cycles at 0.5 C, the electrode maintained an areal capacity of 4.31 mAh cm^{-2}, involving an 83% capacity retention, which is comparable to that of commercial Li-ion batteries (4 mAh cm^{-2}).

Furthermore, a series of electrochemical tests of S@Ni-MOF-1D electrodes were conducted with a sulfur loading of 4.3 mg cm^{-2} (Figure S24). Galvanostatic charge/discharge curves of S@Ni-MOF-1D electrodes showed clear charge/discharge plateaus at the various current rates tested, up to 3C. S@Ni-MOF-1D electrodes delivered a high average initial discharge capacity of 1248 mAh g^{-1}, corresponding to an areal capacity of 5.37 mAh cm^{-2}. Even at a high current rate of 3 C, S@Ni-MOF-1D electrodes still displayed a discharge capacity of 490 mAh g^{-1}, with an areal capacity of 2.11 mAh cm^{-2}. This excellent rate performance at a high sulfur loading is attributed to the high electrical conductivity of π-d Ni-based conjugated coordination polymer.

Figure 5h displays the long-term cycling performance of cells based on S@Ni-MOF-1D electrodes with 4.3 mg cm^{-2} of sulfur. After 450 cycles, the discharge capacity was maintained at 573 mAh g^{-1}, involving an 81.3% capacity retention, *i.e.* a 0.041% average capacity loss per cycle. Besides, S@Ni-MOF-1D electrodes were characterized by a high and stable coulombic efficiency at 99.6%.

Beyond increasing the amount of S@Ni-MOF-1D at the electrode to increase the energy density, we also tested higher S loadings within the host material. Figure S25 displays the cycling stability of a cell based on a S@Ni-MOF-1D composite containing an 81% sulfur loading, as

measured by TGA (Figure S25a). This higher sulfur loading at the composite level translates into a 65% sulfur content at the electrode level (not considering the current collector). At this higher sulfur content, the electrode achieved an initial capacity of 815 mAh g^{-1} at 1 C. After 250 cycles at 1 C, the electrode still maintained a capacity of 695 mAh g^{-1}, which represents an 85.3 capacity retention.

Electrochemical results of S@Ni-MOF-1D cathodes for LSBs are compared to other state-of-the-art MOF-based materials in Table S2 (Supporting Information). To illustrate the favourable electrochemical performance of S@Ni-MOF-1D cathodes and the real practical application of related LSBs, one S@Ni-MOF-1D coin cell was used to light up several LED lamps, as observed in the inset of Figure 5h.

Overall, S@Ni-MOF-1D-based cathodes showed an excellent electrochemical performance associated with the following properties: 1) The delocalization of electrons in the π-d system of Ni-MOF-1D provides a superior electrical conductivity, which maximizes the sulfur utilization; 2) The 1D geometry and favourable charge distribution of the Ni-MOF-1D chains provide parallel 1D paths for electron conduction and Li^+ diffusion; and 3) The presence of $Ni-N_4$ centres, which work as efficient active sites to simultaneously immobilize LiPS and promote their redox reactions. All these results indicate that S@Ni-MOF-1D electrodes can definitively help LSBs to reach practical applications.

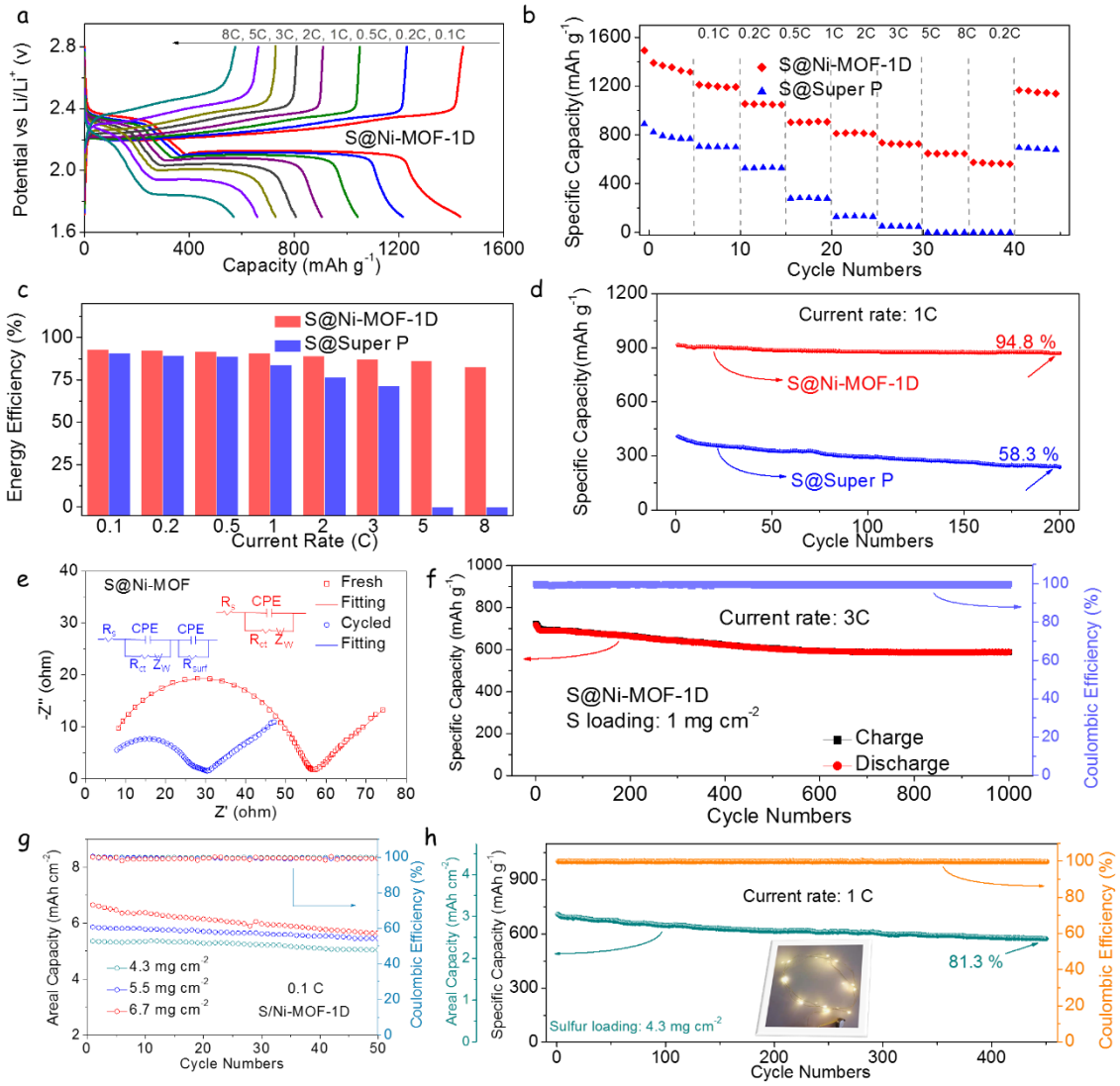

Figure 5. Electrochemical performance of Li-S coin cells. (a) Galvonostatic charge/discharge profile of S@Ni-MOF-1D electrodes at various rates from 0.1 C to 8 C. (b) Rate capabilities of the S@Ni-MOF-1D and S@Super P electrodes at different current rates. (c) Energy efficiency of two different electrodes at various current rates. (d) Capacity retention of S@Ni-MOF-1D and S@Super P electrodes at 1 C over 200 cycles. (e) Nyquist plot of EIS data from S@Ni-MOF-1D electrodes before and after cycling at 1 C. (f) Cycling stability of S@Ni-MOF-1D electrodes at 3 C over 700 cycles. (g) High-loading cycling performances with sulfur loadings of 4.3, 5.5, and 6.7 mg cm^{-2} at 0.1 C of S@Ni-MOF-1D electrodes. (h) Capacity retention of

S@Ni-MOF-1D electrodes with a high sulfur loading of 4.3 mg cm^{-2} at 1 C. Inset shows the digital photograph of LED lamps powered by one S@Ni-MOF-1D Li–S coin cell.

3. Conclusion

In summary, a high conductivity 1D Ni-MOF was rationally designed, engineered, characterized, and tested as an efficient sulfur host for LSBs. Within this material, a π-d hybridization enables the delocalization of a high density of electrons, which provides a metallic character. The associated high electrical conductivity of Ni-MOF-1D allows overcoming the insulating nature of S, Li_2S and most polar S-based electrodes. Besides, the dissolution of LiPS into the electrolyte is largely prevented by the strong interaction between Ni-MOF-1D and LiPS. In addition, within this structure, the Ni-N coordination centres serve as a bifunctional electrocatalyst to facilitate both the formation and the decomposition of Li_2S during discharge and charge processes, respectively. As a result, S@Ni-MOF-1D delivered impressive rate performance with 575 mAh g^{-1} at 8 C, and excellent long-term cycling stability with a minor capacity decay of 0.018% per cycle over 1000 cycles at 3 C. Even at a high sulfur loading of 6.7 mg cm^{-2}, S@Ni-MOF-1D cathodes deliver a remarkable areal capacity of 6.63 mAh cm^{-2} that can meet the needs of commercial LIBs (4 mAh cm^{-2}). This work demonstrated Ni-MOF-1D as an excellent sulfur host, acting as multifunctional polysulfide regulators to chemically adsorb LiPS, accelerate Li^+ diffusion, and catalyze the LiPS conversion reactions. More generally, this work presented new insights and deepen understanding of π-d conjugated MOFs and demonstrated their potential as cathode host material in LSBs.

Supporting Information

Supporting Information is available from the Wiley Online Library or from the author.

Acknowledgements

This work was supported by the European Regional Development Funds and by the Spanish Ministerio de Economía y Competitividad through the projects ENE2016- 77798-C4-3-R, and PID2020-116093RB-C43. D. Yang and C. Zhang thank the China Scholarship Council for the scholarship support. M. Tang thanks the financial support from the National Natural Science Foundation of China (Grants 21974007 and U1930401). Z. Liang acknowledges funding from MINECO SO FPI PhD grant (SEV-2013-0295-17-1). P. Tang acknowledges the Humboldt Research Fellowship. Authors acknowledge funding from Generalitat de Catalunya 2017 SGR 327 and 2017 SGR 1246. ICN2 acknowledges the support from the Severo Ochoa Programme (MINECO, grant no. SEV-2017-0706). IREC and ICN2 are both funded by the CERCA Programme/Generalitat de Catalunya. This work was supported by Fundamental Research Funds for the Central Universities (buctrc202112). J. Llorca is a Serra Húnter Fellow and is grateful to MICINN/FEDER RTI2018-093996-B-C31, GC 2017 SGR 128 and to ICREA Academia program. This project has received funding from the European Union's Horizon 2020 research and innovation programme under grant agreement No 823717 – ESTEEM3. Part of the present work has been performed in the framework of Universitat Autònoma de Barcelona Materials Science PhD program. The authors are thankful for the support of the BSRF (Beijing Synchrotron Radiation Facility) during the XAFS measurements at the beamline 1W1B, 4B7A, 4B7B, 4B9B, and Shanghai Synchrotron Radiation Facility (SSRF).

Received: ((will be filled in by the editorial staff))
Revised: ((will be filled in by the editorial staff))
Published online: ((will be filled in by the editorial staff))

References

[1] P. G. Bruce, S. A. Freunberger, L. J. Hardwick, J. M. Tarascon, *Nat. Mater.* **2011**, *11*, 19-29.

[2] G. Zhou, D.-W. Wang, F. Li, P.-X. Hou, L. Yin, C. Liu, G. Q. Lu, I. R. Gentle, H.-M. Cheng, *Energy Environ. Sci.* **2012**, *5*, 8901.

[3] Z. Li, B. Y. Guan, J. Zhang, X. W. Lou, *Joule* **2017**, *1*, 576-587.

[4] Z. Xiao, Z. Yang, L. Wang, H. Nie, M. Zhong, Q. Lai, X. Xu, L. Zhang, S. Huang, *Adv. Mater.* **2015**, *27*, 2891-2898.

[5] X. Chen, H.-J. Peng, R. Zhang, T.-Z. Hou, J.-Q. Huang, B. Li, Q. Zhang, *ACS Energy Letters* **2017**, *2*, 795-801.

[6] Y. Yang, G. Zheng, Y. Cui, *Chem.Soc.Rev.* **2013**, *42*, 3018-3032.

[7] X. Liang, Y. Rangom, C. Y. Kwok, Q. Pang, L. F. Nazar, *Adv. Mater.* **2017**, *29*, 1603040.

[8] A. Shyamsunder, W. Beichel, P. Klose, Q. Pang, H. Scherer, A. Hoffmann, G. K. Murphy, I. Krossing, L. F. Nazar, *Angew. Chem., Int. Ed.* **2017**, *56*, 6192-6197.

[9] Z. Sun, J. Zhang, L. Yin, G. Hu, R. Fang, H. M. Cheng, F. Li, *Nat. Commun.* **2017**, *8*, 14627.

[10] J. Xie, B. Q. Li, H. J. Peng, Y. W. Song, M. Zhao, X. Chen, Q. Zhang, J. Q. Huang, *Adv. Mater.* **2019**, *31*, e1903813.

[11] L. Ji, M. Rao, S. Aloni, L. Wang, E. J. Cairns, Y. Zhang, *Energy Environ. Sci.* **2011**, *4*, 5053.

[12] Z. Li, J. Zhang, B. Guan, D. Wang, L. M. Liu, X. W. Lou, *Nat. Commun.* **2016**, *7*, 13065.

[13] C. Zu, A. Manthiram, *Adv. Energy Mater.* **2013**, *3*, 1008-1012.

[14] J. Zhang, Z. Li, Y. Chen, S. Gao, X. W. D. Lou, *Angew. Chem. Int. Ed.* **2018**, *130*, 11110-11114.

[15] Y. Zhong, D. Chao, S. Deng, J. Zhan, R. Fang, Y. Xia, Y. Wang, X. Wang, X. Xia, J. Tu, *Adv. Funct. Mater.* **2018**, *28*, 1706391.

[16] Z. Cheng, Z. Xiao, H. Pan, S. Wang, R. Wang, *Adv. Energy Mater.* **2018**, *8*, 1702337.

[17] D. Cai, B. Liu, D. Zhu, D. Chen, M. Lu, J. Cao, Y. Wang, W. Huang, Y. Shao, H. Tu, W.

Han, *Adv. Energy Mater.* **2020**, *10*, 1904273.

[18] Z. Ye, Y. Jiang, L. Li, F. Wu, R. Chen, *Adv. Mater.* **2020**, *32*, e2002168.

[19] S. Bai, X. Liu, K. Zhu, S. Wu, H. Zhou, *Nat. Energy*. **2016**, *1*, 16094.

[20] M. Rana, H. A. Al-Fayaad, B. Luo, T. Lin, L. Ran, J. K. Clegg, I. Gentle, R. Knibbe, *Nano Energy* **2020**, *75*, 105009.

[21] J. Zheng, J. Tian, D. Wu, M. Gu, W. Xu, C. Wang, F. Gao, M. H. Engelhard, J. G. Zhang, J. Liu, J. Xiao, *Nano Lett.* **2014**, *14*, 2345-2352.

[22] Z. Wang, B. Wang, Y. Yang, Y. Cui, Z. Wang, B. Chen, G. Qian, *ACS Appl. Mater. Interfaces* **2015**, *7*, 20999-21004.

[23] D. Cai, M. Lu, Li, J. Cao, D. Chen, H. Tu, J. Li, W. Han, *Small* **2019**, *15*, e1902605.

[24] M. Tang, S. Zhu, Z. Liu, C. Jiang, Y. Wu, H. Li, B. Wang, E. Wang, J. Ma, C. Wang, *Chem* **2018**, *4*, 2600-2614.

[25] V. Rubio-Gimenez, M. Galbiati, J. Castells-Gil, N. Almora-Barrios, J. Navarro-Sanchez, G. Escorcia-Ariza, M. Mattera, T. Arnold, J. Rawle, S. Tatay, E. Coronado, C. Marti-Gastaldo, *Adv. Mater.* **2018**, *30*, 1704291.

[26] J. H. Dou, L. Sun, Y. Ge, W. Li, C. H. Hendon, J. Li, S. Gul, J. Yano, E. A. Stach, M. Dinca, *J. Am. Chem. Soc.* **2017**, *139*, 13608-13611.

[27] Y. Jiang, I. Oh, S. H. Joo, O. Buyukcakir, X. Chen, S. H. Lee, M. Huang, W. K. Seong, S. K. Kwak, J. W. Yoo, R. S. Ruoff, J. Am. Chem. Soc. **2019**, *141*, 16884-16893.

[28] D. Xing, Y. Wang, P. Zhou, Y. Liu, Z. Wang, P. Wang, Z. Zheng, H. Cheng, Y. Dai, B. Huang, *Appl. Catal., B* **2020**, *278*, 119295.

[29] Z. Liang, D. Yang, P. Tang, C. Zhang, J. Jacas Biendicho, Y. Zhang, J. Llorca, X. Wang, J. Li, M. Heggen, J. David, R. E. Dunin‐Borkowski, Y. Zhou, J. R. Morante, A. Cabot, J. Arbiol, *Adv. Energy Mater.* **2020**, *11*, 2003507.

[30] X. Hao, Z. Cui, J. Zhou, Y. Wang, Y. Hu, Y. Wang, Z. Zou, *Nano Energy* **2018**, *52*, 105-116.

[31] L. Wang, Y. Ni, X. Hou, L. Chen, F. Li, J. Chen, *Angew. Chem., Int. Ed.* **2020**, *59*, 22126-22131.

[32] Y. Guo, Z. Wang, X. Lu, J. Lu, K. Rabia, H. Chen, R. Hu, H. Tang, Q. Zhang, Z. Li,

Chem Commun. **2020**, *56*, 1980.

[33] G. Cai, P. Cui, W. Shi, S. Morris, S. N. Lou, J. Chen, J. H. Ciou, V. K. Paidi, K. S. Lee, S. Li, P. S. Lee, *Adv. Sci.* **2020**, *7*, 1903109.

[34] X. Xiong, C. Mao, Z. Yang, Q. Zhang, G. I. N. Waterhouse, L. Gu, T. Zhang, *Adv. Energy Mater.* **2020**, *10*, 2002928.

[35] K. Jiang, S. Siahrostami, T. Zheng, Y. Hu, S. Hwang, E. Stavitski, Y. Peng, J. Dynes, M. Gangisetty, D. Su, K. Attenkofer, H. Wang, *Energy Environ. Sci.* **2018**, *11*, 893-903.

[36] L. Zhang, D. Liu, Z. Muhammad, F. Wan, W. Xie, Y. Wang, L. Song, Z. Niu, J. Chen, *Adv. Mater.* **2019**, *31*, e1903955.

[37] C. Zhao, X. Dai, T. Yao, W. Chen, X. Wang, J. Wang, J. Yang, S. Wei, Y. Wu, Yadong Li, *J. Am. Chem. Soc.* **2017**, *139*, 8078–8081.

[38] A. Frank, A. Berkefeld, M. Drexler, H. M. Möller, T. E. Exner, *Int. J. Quantum Chem.* **2013**, *113*, 1787-1793.

[39] S. A. Rouf, V. B. Jakobsen, J. Mares, N. D. Jensen, C. J. McKenzie, J. Vaara, U. G. Nielsen, *Solid State Nucl. Magn. Reson.* **2017**, *87*, 29-37.

[40] A. Ishitani, S. Nagakura, *Mol. Phys.* **1967**, *12*, 1-12.

[41] A. N. Ponomaryov, N. Kim, J. Hwang, H. Nojiri, J. van Tol, A. Ozarowski, J. Park, Z. Jang, B. Suh, S. Yoon, K. Y. Choi, *Chem. Asian J.* **2013**, *8*, 1152-1159.

[42] Z. Zhao, T. Yu, S. Zhang, H. Xu, G. Yang, Y. Liu, *J. Mater. Chem. A.* **2019**, *7*, 405-411.

[43] J. P. Piquemal, J. Pilmé, O. Parisel, H. Gérard, I. Fourré, J. Bergès, C. Gourlaouen, A. De La Lande, M. C. Van Severen, B. Silvi, *Int. J. Quantum Chem.* **2008**, *108*, 1951-1969.

[44] M. Xue, Y. Zhou, J. Geng, P. Zeng, Y. Xu, Y. Wang, W. Tang, P. Wu, S. Wei, Yiming Zhou, *RSC Adv.* **2016**, *6*, 91179-91184.

[45] T. Lei, W. Chen, J. Huang, C. Yan, H. Sun, C. Wang, W. Zhang, Y. Li, J. Xiong, *Adv. Energy Mater.* **2017**, *7*, 1601843.

[46] D. Yang, C. Zhang, J. J. Biendicho, X. Han, Z. Liang, R. Du, M. Li, J. Li, J. Arbiol, J. Llorca, Y. Zhou, J. R. Morante, A. Cabot, *ACS Nano* **2020**, *14*, 15492-15504.

[47] Z. Du, X. Chen, W. Hu, C. Chuang, S. Xie, A. Hu, W. Yan, X. Kong, X. Wu, H. Ji, L. J.

Wan, *J. Am. Chem. Soc.* **2019**, *141*, 3977-3985.

[48] H. Lin, L. Yang, X. Jiang, G. Li, T. Zhang, Q. Yao, G. W. Zheng, J. Y. Lee, *Energy Environ. Sci.* **2017**, *10*, 1476-1486.

[49] C. Zhang, R. Du, J. J. Biendicho, M. Yi, K. Xiao, D. Yang, T. Zhang, X. Wang, J. Arbiol, J. Llorca, Y. Zhou, J. R. Morante, A. Cabot, *Adv. Energy Mater.* **2021**, *11*, 2100432.

[50] S. S. Zhang, *J. Power Sources* **2013**, *231*, 153-162.

[51] D. Moy, A. Manivannan, S. R. Narayanan, *J. Electrochem. Soc.* **2014**, *162*, A1-A7.

[52] Y. Tian, G. Li, Y. Zhang, D. Luo, X. Wang, Y. Zhao, H. Liu, P. Ji, X. Du, J. Li, Z. Chen, *Adv. Mater.* **2020**, *32*, e1904876.

[53] Z. Yuan, H. J. Peng, T. Z. Hou, J. Q. Huang, C. M. Chen, D. W. Wang, X. B. Cheng, F. Wei, Q. Zhang, *Nano Lett.* **2016**, *16*, 519-527.

[54] G. Zhou, H. Tian, Y. Jin, X. Tao, B. Liu, R. Zhang, Z. W. Seh, D. Zhuo, Y. Liu, J. Sun, J. Zhao, C. Zu, D. S. Wu, Q. Zhang, Y. Cui, *Proc. Natl. Acad. Sci. USA* **2017**, *114*, 840-845.

[55] X. Zhu, W. Zhao, Y. Song, Q. Li, F. Ding, J. Sun, L. Zhang, Z. Liu, *Adv. Energy Mater.* **2018**, *8*, 1800201.

[56] S. Niu, S.-W. Zhang, R. Shi, J. Wang, W. Wang, X. Chen, Z. Zhang, J. Miao, A. Amini, Y. Zhao, C. Cheng, *Energy Storage Mater.* **2020**, *33*, 73-81.

[57] D. Su, M. Cortie, H. Fan, G. Wang, *Adv. Mater.* **2017**, *29*, 1700587.

[58] J. Zhou, R. Li, X. Fan, Y. Chen, R. Han, W. Li, J. Zheng, B. Wang, X. Li, *Energy Environ. Sci.* **2014**, *7*, 2715-2724.

[59] F. Y. Fan, W. C. Carter, Y. M. Chiang, *Adv. Mater.* **2015**, *27*, 5203-5209.

[60] A. Eftekhari, *Sustainable Energy Fuels* **2017**, *1*, 2053-2060.

[61] T. Zhou, W. Lv, J. Li, G. Zhou, Y. Zhao, S. Fan, B. Liu, B. Li, F. Kang, Q.-H. Yang, *Energy Environ. Sci.* **2017**, *10*, 1694-1703.

[62] C.-S. Cheng, S.-H. Chung, *Chem. Eng. J.* **2022**, *429*, 132257.

[63] Ş. Sörgel, O. Kesten, A. Wengel, T. Sörgel, *Energy Storage Mater.* **2018**, *10*, 223.

Rationally designed multifunctional polysulfide mediators based on a novel one dimensional (1D) π-d conjugated Ni-based MOF (Ni-MOF-1D) are demonstrated as excellent cathode materials in lithium-sulfur batteries (LSBs), realizing the adsorption-catalysis-conversion of polysulfides, and thus batteries with exceptional lifespan are delivered.

Keyword: Lithium-sulfur battery

Dawei Yang+, Zhifu Liang+, Pengyi Tang+, Chaoqi Zhang, Mingxue Tang, Qizhen Li, Jordi Jacas Biendicho, Junshan Li, Marc Heggen, Rafal E. Dunin-Borkowski, Ming Xu*, Jordi Llorca, Jordi Arbiol*, Joan Ramon Morante, Shu-Lei Chou*, Andreu Cabot*

A High Conductivity One-Dimensional π-d Conjugated Metal-Organic Framework with Efficient Polysulfide Trapping-Diffusion-Catalysis in Lithium-Sulfur Batteries

ToC figure:

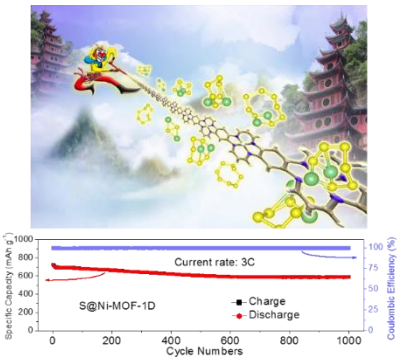

Supporting Information

A High Conductivity One-Dimensional π-d Conjugated Metal-Organic Framework with Efficient Polysulfide Trapping-Diffusion-Catalysis in Lithium-Sulfur Batteries

Dawei Yang+, Zhifu Liang+, Pengyi Tang+, Chaoqi Zhang, Mingxue Tang, Qizhen Li, Jordi Jacas Biendicho, Junshan Li, Marc Heggen, Rafal E. Dunin-Borkowski, Ming Xu, Jordi Llorca, Jordi Arbiol*, Joan Ramon Morante, Shu-Lei Chou*, Andreu Cabot**

D. W. Yang, Z. F. Liang, C. Q. Zhang, Dr. J. J. Biendicho, Prof. J. R. Morante, Prof. A. Cabot
Catalonia Institute for Energy Research - IREC,
Sant Adrià de Besòs, Barcelona, 08930, Spain
Email: acabot@irec.cat

D. W. Yang, C. Q. Zhang, Prof. J. R. Morante
Department of Electronic and Biomedical Engineering
Universitat de Barcelona, 08028 Barcelona, Spain

Z. F. Liang, Prof. J. Arbiol
Catalan Institute of Nanoscience and Nanotechnology (ICN2)
CSIC and BIST, Campus UAB, Bellaterra, 08193 Barcelona, Spain
Email: arbiol@icrea.cat

Dr. P. Y Tang, Dr. M Heggen, Prof. R E. Dunin-Borkowski
Ernst Ruska-Centre for Microscopy and Spectroscopy with Electrons and Peter Grünberg Institute Forschungszentrum Jü lich GmbH 52425 Jülich, Germany

Dr. P. Y Tang
State Key Laboratory of Information Functional Materials, 2020 X-Lab, ShangHai Institute of Microsystem and Information Technology, Chinese Academy of Sciences, Shanghai, P. R. China

Prof. M. X. Tang
Center for High Pressure Science and Technology Advanced Research, Beijing 100094, China

Q. Z. Li
Department of Biomedical Engineering, Southern University of Science and Technology (SUSTech), Shenzhen, Guangdong, 518055, China

Dr. J. S. Li

Institute of Advanced Study, Chengdu University, Chengdu 610106, China

Prof. J. Llorca
Institute of Energy Technologies, Department of Chemical Engineering and Barcelona Research Center in Multiscale Science and Engineering, Universitat Politècnica de Catalunya, EEBE, 08019, Barcelona, Spain

Prof. M. Xu
State Key Laboratory of Chemical Resource Engineering, Beijing University of Chemical Technology, Beijing 100029, P. R. China
Email: mingxu@mail.buct.edu.cn

Prof. S. L. Chou
Institute for Carbon Neutralization, College of Chemistry and Materials Engineering, Wenzhou University, Wenzhou, Zhejiang 325035, China
E-mail: chou@wzu.edu.cn

Prof. J. Arbiol, Prof. A. Cabot
ICREA
Pg. Lluís Companys 23, 08010 Barcelona, Spain
+ These authors contributed equally to this work

Experimental Procedures

Chemicals: 1,3-dioxolane (DOL, 99.5%), lithium nitrate ($LiNO_3$, 99.98%), lithium sulfide (Li_2S, 99.9%), poly(vinylidene fluoride) (PVDF, 99%), and Super P (99%) were purchased from Alfa Aesar. 1,2,4,5-benzenetetramine tetrahydrochloride (≥96%), 1,1,3,3-tetramethoxypropane (99%), nickel acetate tetrahydrate (99.99%), triethylamine (Et_3N, 99.5%), N-methyl-2-pyrrolidone (NMP, 99.99%), sublimed sulfur (99.98%), and carbon disulfide (CS_2, 99.9%) were purchased from Sigma-Aldrich. Lithium bis(trifluoromethanesulfonyl) imide (LiTFSI, 99%) was purchased from Acros Organics and 1,2-dimethoxymethane (DME, 99%) was from Honeywell. All chemicals were used without further purification.

Synthesis of Ni-MOF-1D: The synthesis of Ni-MOF-1D is based on the following steps [6]: First, Ni^{2+} ions are coordinated with two 1,2,4,5-benzenetetramine. Then, the 1,1,3,3-tetramethoxypropane is hydrolyzed to malondialdehyde. Finally, the malondialdehyde is used as linker to react with the two 1,2,4,5-benzenetetramine:

First,

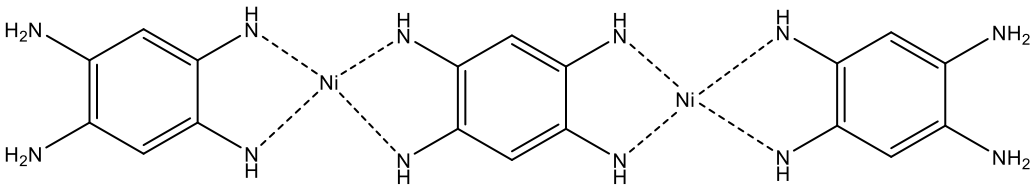

Then,

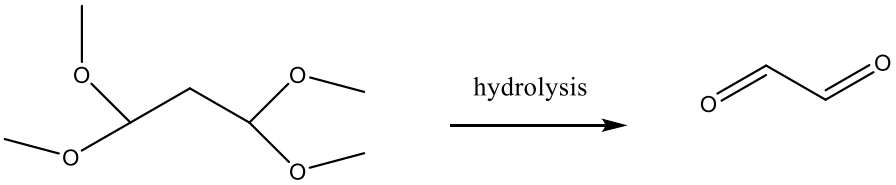

and finally,

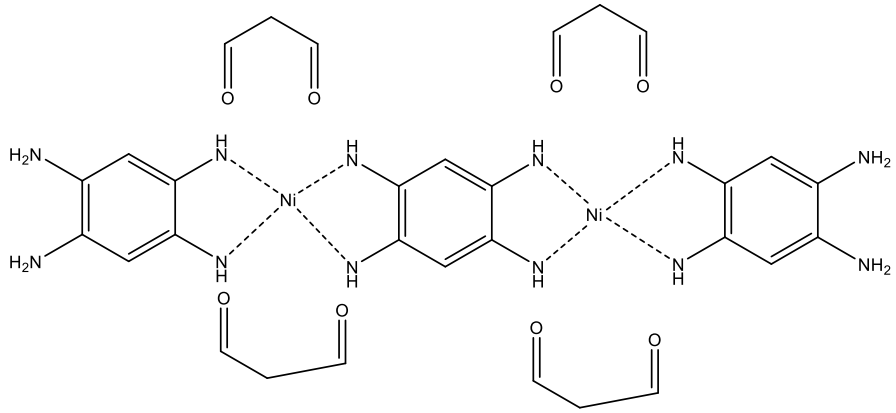

More in detail, 1,2,4,5-benzenetetramine tetrahydrochloride (284 mg, 1 mol), 1,1,3,3-tetramethoxypropane (165 μL, 2 mol) and nickel acetate tetrahydrate (248.8 mg, 1 mol) were placed into a 25 mL three-neck flask. Subsequently, 15 mL of water was added. Then the mixture was stirred for half an hour. Then Et_3N (0.55 μL, 4 mol) was added to the above mixture, which was then heated at 100 °C for 24 h with stirring. The obtained precipitate was filtrated by vacuum and then washed with water and a small amount of methanol. The material was vacuum dried for 12 h under 60 °C.

Synthesis of S@Ni-MOF-1D and S@Super P: Typically, Ni-MOF-1D and sulfur powder were well mixed with a weight ratio of 1:3, and then heated at 155 °C for 8 h under Ar protection in a sealed glass bottle. Then the redundant sulfur not incorporated into Ni-MOF-1D was washed by 10 mL CS_2 and ethanol solution (1:4, volume ratio) for several times. For comparison, S@Super P was also prepared by the same method.

Materials Characterization: X-ray diffraction (XRD) patterns were detected using a Bruker AXS D8 Advance X-ray diffractometer with Cu K radiation (λ = 1.5106 Å) operating at 40 kV and 40 mA. The morphology, structure and composition of the samples were characterized by field emission scanning electron microscopy (FE-SEM, ZEISS Auriga) equipped with an energy dispersive X-ray spectroscopy (EDX). High-resolution TEM (HRTEM) studies were carried out using a FEI Tecnai F20 microscope at 200 kV. High angle annular dark-field scanning transmission electron microscopy (HAADF-STEM) images and elemental mapping were obtained in a spherical aberration-corrected transmission electron microscope FEI Titan 80-300 at 300 kV and FEI Titan G2 80-200 ChemiSTEM with four EDX detectors and operated at 200 kV. The Integrated differential phase-contrast STEM (iDPC-STEM) images were obtained under a spherical aberration (Cs)-corrected STEM (FEI Titan Cubed Themis G2 300) operated at 300 kV. X-ray photoelectron spectroscopy (XPS) measurements were conducted by operating at 150 W and a Phoibos 150 MCD-9 detector. X-ray absorption near-edge structure (XANES) and extended X-ray absorption fine structure (FT-EXAFS) were performed at the Beijing Synchrotron Radiation Facility (BSRF). XAFS data were analyzed according to the standard procedures using ATHENA program. The content of sulfur within the cathode composites was estimated by thermogravimetric (TGA) on a PerkinElmer Diamond TG/DTA instrument under nitrogen (N_2) at a heating rate of 10 °C min^{-1}. UV–vis absorption spectrum

was tested using PerkinElmer Lambda 950 UV–vis spectrophotometer. Nitrogen adsorption-desorption isotherms were recorded to calculate the specific surface area and analysis of the pore size distribution by Brunauer-Emmett-Teller method on a Tristar II 3020 Micromeritics system. The well-resolved solid-state Magic Angle Spinning Nuclear Magnetic Resonance (MAS-NMR) spectra were acquired on a Bruker 400 MHz spectrometer with 4.0 mm HX double resonance probe at the ^{1}H and ^{13}C Larmor frequencies of 400.17 and 100.62 MHz, respectively. Continuous-wave electron paramagnetic resonance (CW-EPR) spectrum was acquired on a Bruker EMXmicro spectrometer at X-band (9.5 GHz).

Li-S Cell Assembly and Measurements: S@host composites (S@Ni-MOF-1D, and S@Super P), PVDF binders and Super P (weight ratio =8:1:1) were dispersed in NMP. The obtained slurry was coated on an aluminum foil and vacuum dried at 60 °C overnight. The coated aluminum foil was then punched into small disks with diameter of 12 mm. Sulfur loading was around 1.0-1.2 mg cm^{-2}. CR2032 coin-type cells were assembled in an Ar-filled glove box with lithium foils as counter electrodes, Celgard 2400 membranes as separators, and 1.0 M LiTFSI in DOL/DME solvent (1:1 vol%) with 0.2 M $LiNO_3$ additive as the electrolyte. The electrolyte/sulfur ratio was controlled to be about 20 μL mg^{-1} for the common coin cells. The galvanostatic charge/discharge (GCD) measurements were conducted at a voltage window of 1.7-2.8 V vs. Li^{+}/Li on a Neware BTS4008 battery tester with different C rates. The battery tester BCS-810 from Bio Logic was used to carry out the cyclic voltammetry (CV) measurements at a scan rate of 0.1-0.5 mV s^{-1}, and the electrochemical impedance spectroscopy (EIS) tests with a voltage amplitude of 10 mV in the frequency range 0.01-10^{5} Hz.

Synthesis of Li_2S_4 solutions for adsorption test: Sulfur and Li_2S with a molar ratio of 3:1 dissolved in an appropriate amount of DME/DOL (volume ratio of 1:1) solution under continuous stirring overnight, eventually obtaining a homogeneous dark brown solution. To evaluate the absorption ability for polysulfide, 15 mg of S@Ni-MOF-1D and S@Super P were added to 3.0 mL 10×10^{-3} M Li_2S_4 solution under Ar atmosphere, respectively.

Symmetric Cell Assembly and Measurements: Electrodes for symmetric cells were prepared by using the same process as that for LSBs. Two pieces of the same electrode (average loading about 0.5 mg cm^{-2}) were used as working and counter electrodes with 40 μL of electrolyte containing 0.5 mol L^{-1} Li_2S_6 and 1 mol L^{-1} LiTFSI dissolved in DOL/DME (v/v = 1/1). For

comparison, symmetric cells with electrolyte 1 mol L^{-1} LiTFSI dissolved in DOL/DME (v/v = 1/1) were also assembled and tested under CR2032 coin cells. The CV measurements for all the symmetric cells were performed at a scan rate of 20 mV s^{-1} in a voltage window between -1.0 and 1.0 V.

Measurement of Nucleation of Li_2S: Nucleation and dissolution of Li_2S were tested in 2032 coin cells to investigate the liquid-solid reaction kinetics. A certain amount of host materials loaded on the carbon papers applied as work electrode. Li foil worked as the counter electrode. The catholyte consisted of 20 μL of 0.25 M Li_2S_8 and 1.0 M LiTFSI in tetraethylene glycol dimethyl ether solution. In the case of anolyte, it contained 20 μL of a 1.0 M LiTFSI solution without Li_2S_8. The cells were first discharged at a current of 0.112 mA to 2.19 V and then hold the voltage at 2.05 V until the current decreased to 10^{-2} mA for Li_2S nucleation and growth.

DFT calculations

Density functional theory (DFT) calculations were performed to understand the interactions of LiPS species with Ni-MOF-1D cathode hosts. Spin-polarized DFT calculations were performed in the VASP code using projector augmented wave (PAW) pseudopotentials.[1,2] The SCAN meta-GGA functional was used in this system for obtaining the accurate absorbing configurations and energy as it takes up to 17 interaction force in to consideration between atoms,[3,4] which provides an accurate description of short, intermediate and long-range van der Waals interactions.[5]

Ni-MOF-1D was built with a vacuum layer with the Z-axis by 0.15 nm and the Y-axis by 15 nm. The free energy stage for each absorbent was calculated by following equation, taking *-Li_2S_2→*-Li_2S_4:

$$E_{free*\text{-}Li2S2\rightarrow *\text{-}Li2S4}=E_{free*\text{-}Li2S4}- E_{free*\text{-}Li2S2}- 2*1/8*E_{freeS8}$$

where，$E_{free*\text{-}Li2S2\rightarrow *\text{-}Li2S4}$ is the free energy variation for the reaction of *-Li_2S_2→*-Li_2S_4, the $E_{free*\text{-}Li2S4}$, the $E_{free*\text{-}Li2S2}$ and the E_{freeS8}, are the absolute DFT obtained energy after considering ZPE, TS correction. In terms of the energy of Li ions, it was taken the 1/4 Li bulk (primitive cell with 4 Li atoms). Band structure was calculated with HSE06 functional accuracy.

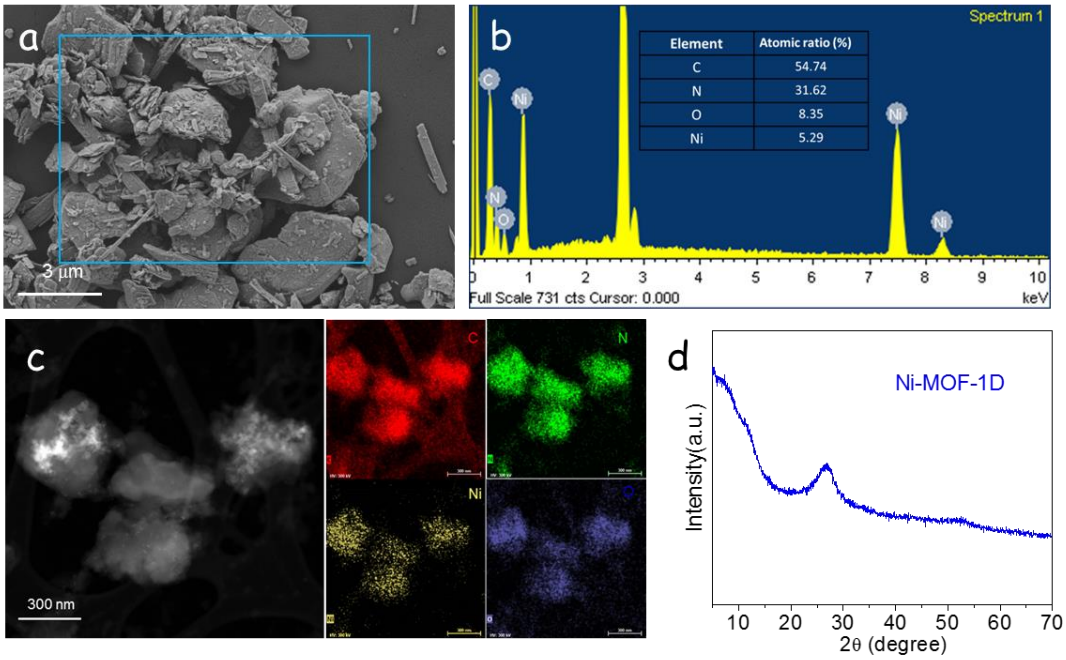

Figure S1. (a,b) SEM image and EDX spectrum of Ni-MOF-1D sample. (c) High magnification STEM-HAADF image and EDX elemental mapping showing the elemental distribution in a Ni-MOF-1D sample. (d) XRD pattern of Ni-MOF-1D.

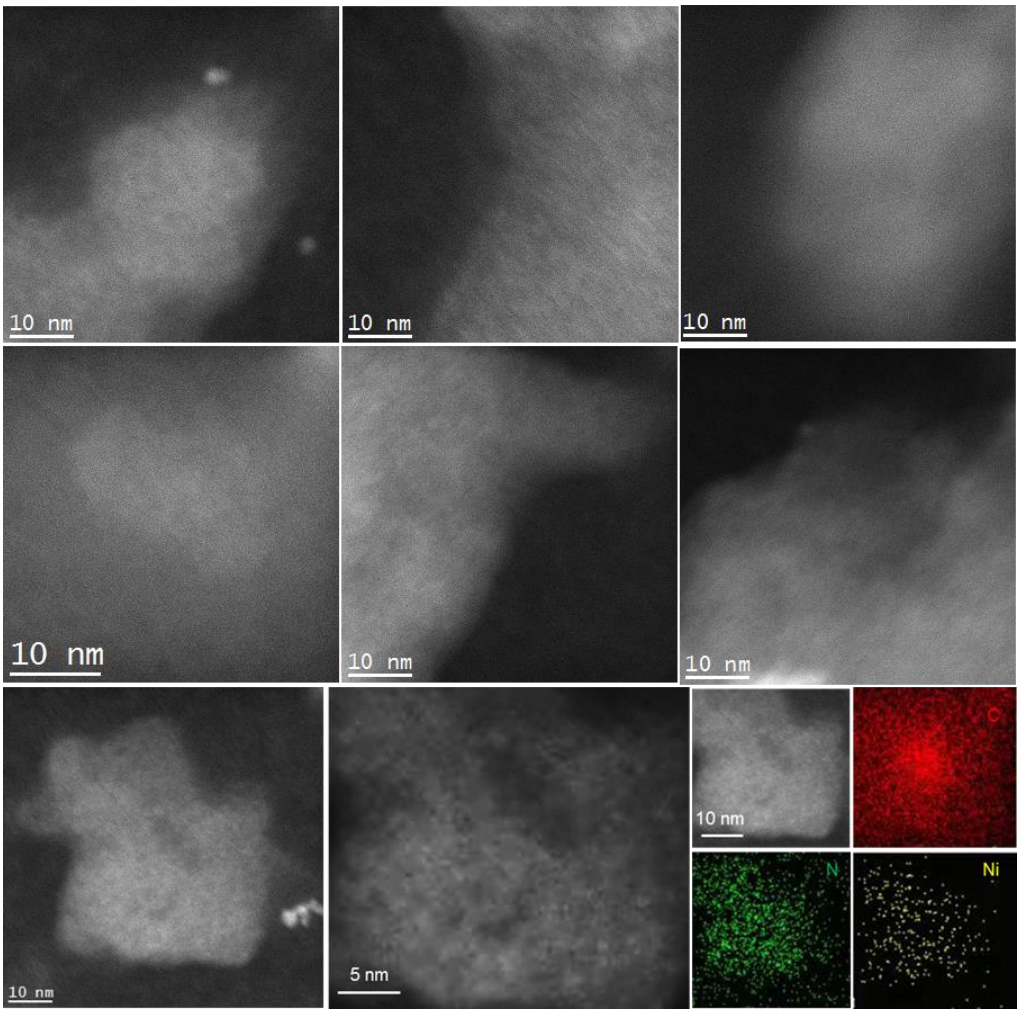

Figure S2. High magnification HAADF-STEM images and detailed STEM-EDX elemental maps of a Ni-MOF-1D catalyst.

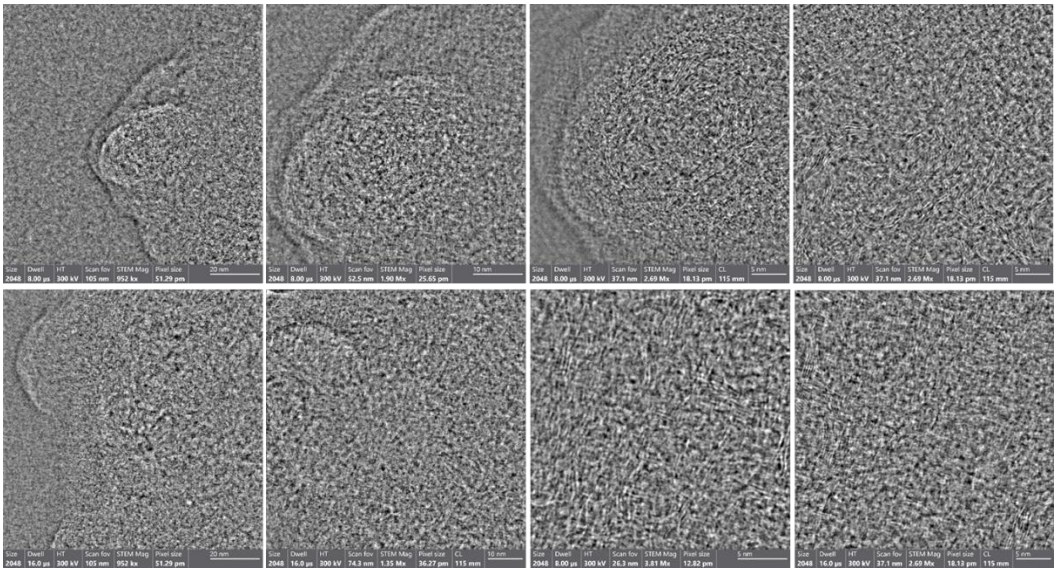

Figure S3. iDPC-STEM images of Ni-MOF-1D with different magnifications.

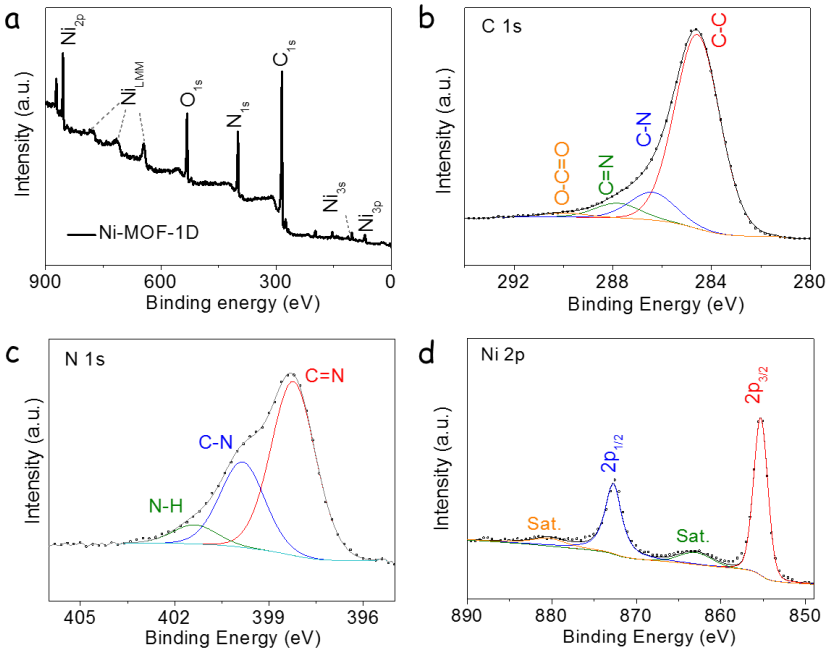

Figure S4. (a) XPS survey spectrum of Ni-MOF-1D. (b-d) High resolution XPS spectra of b) C 1s, c) N 1s, and d) Ni 2p.

Table S1 Detailed EXAFS fitting model and parameters of Ni-MOF-1D.

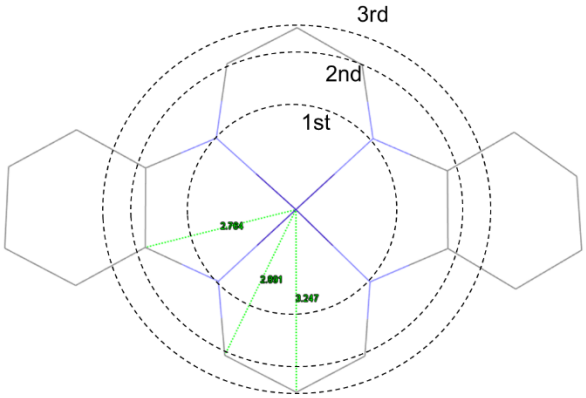

	N	*R* / Å	σ	ΔE / eV
N (1st)	4	1.86	0.002	-8.37
C (2nd)	8	2.73	0.012	-8.37
C (3rd)	2	3.08	0.035	-8.37

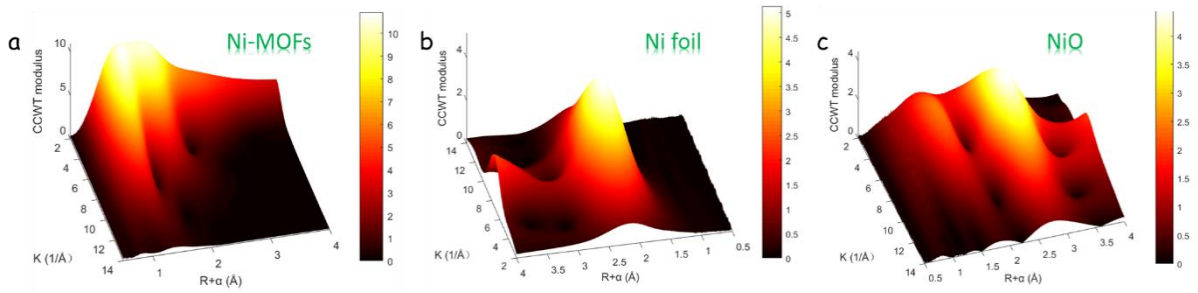

Figure S5. Wavelet transform (WT) analysis of (a) Ni-MOF-1D, (b) Ni foil, and (c) NiO.

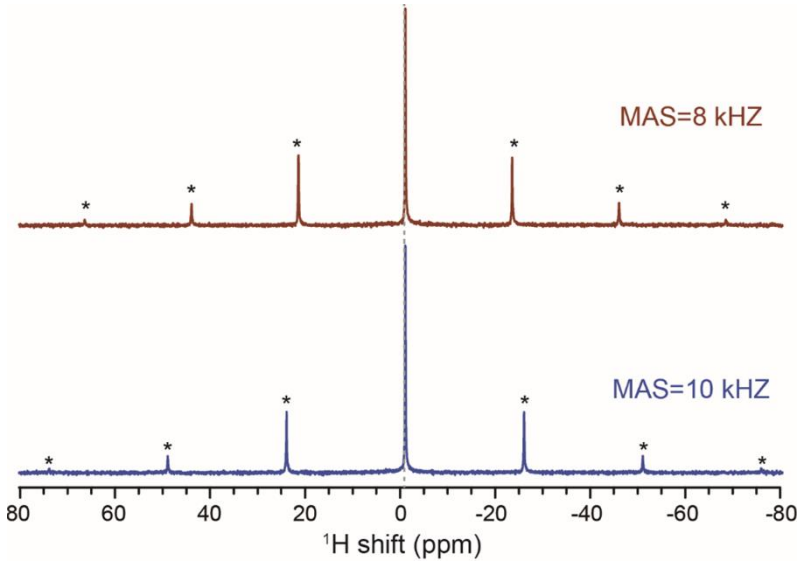

Figure S6. ^{1}H NMR spectra of the obtained sample of Ni-MOF-1D.

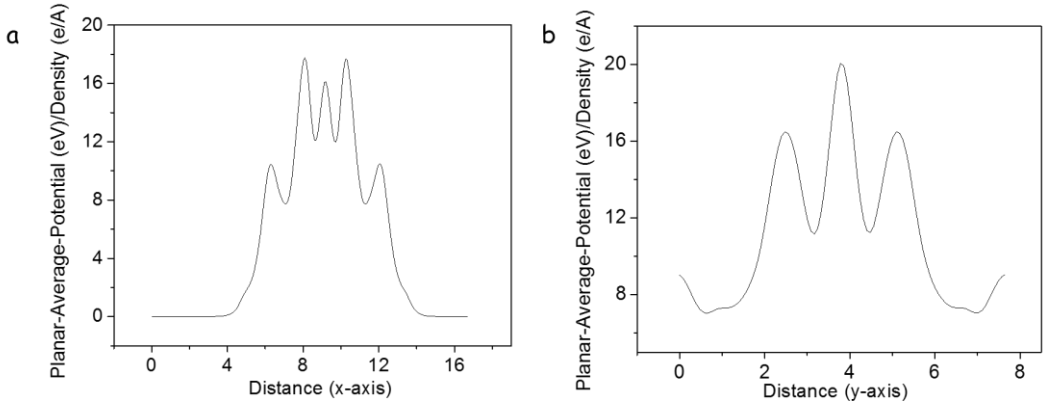

Figure S7. (a) Projected integral of the charge density in the non-periodic direction. (b) Projected integral of the charge density in the periodic direction of Ni-MOF-1D.

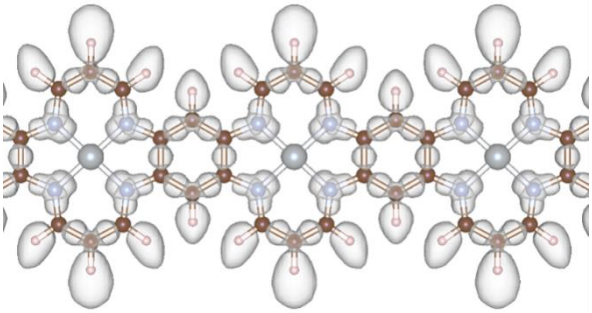

Figure S8. Calculated electron localization function (ELF) of Ni-MOF-1D.

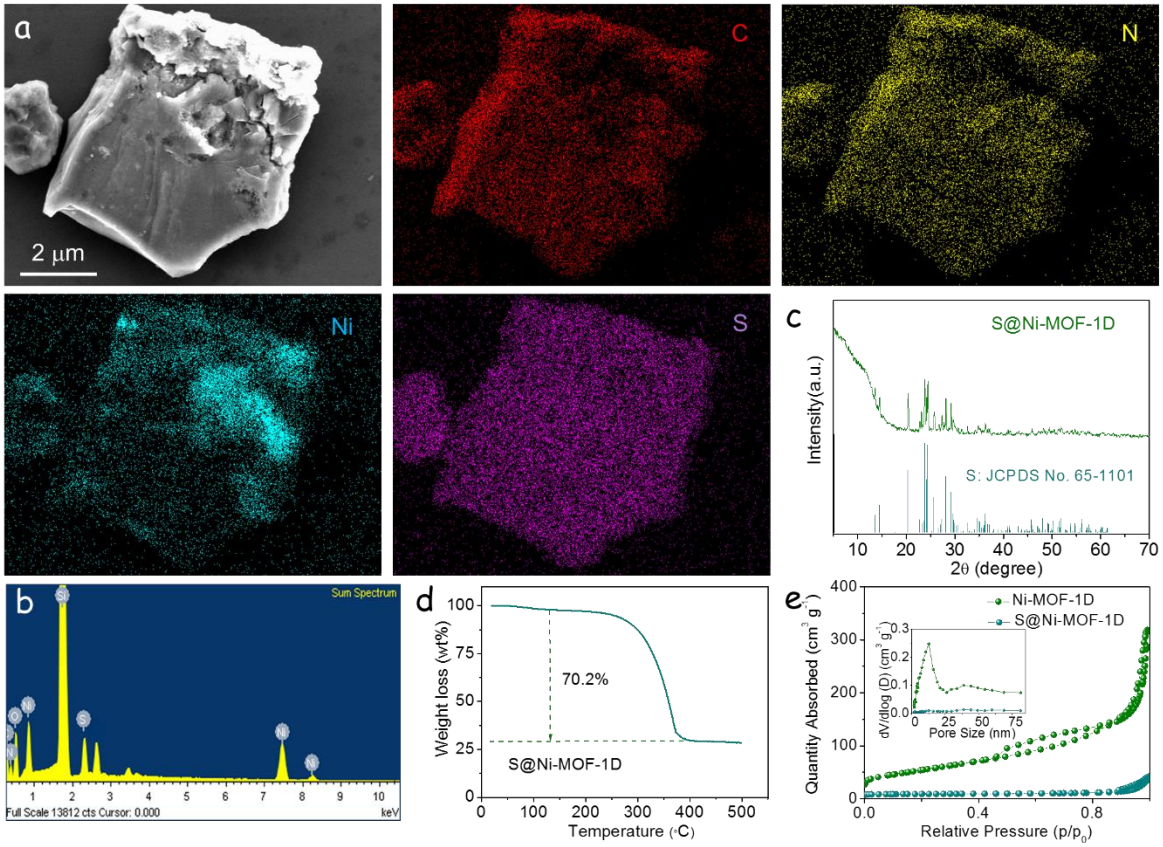

Figure S9. (a) SEM-EDX compositional maps and (b) EDX spectra of S@Ni-MOF-1D. (c) XRD pattern of S@Ni-MOF-1D. (d) TGA profile from S@Ni-MOF-1D measured in N_2 atmosphere. (e) N_2 adsorption-desorption isotherms of Ni-MOF-1D and S@Ni-MOF-1D. Inset: Pore size distribution of Ni-MOF-1D and S@Ni-MOF-1D.

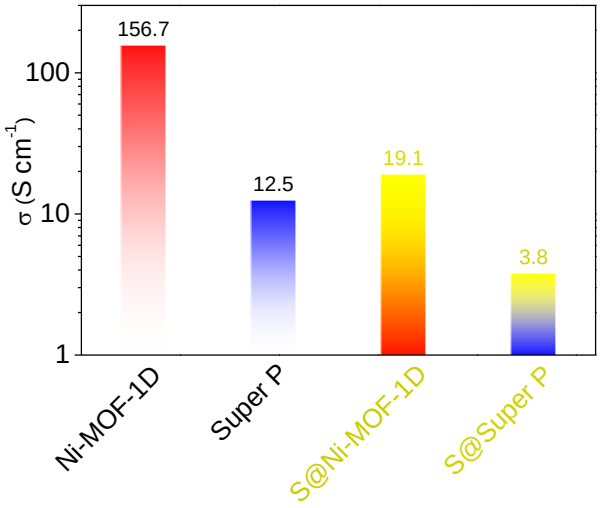

Figure S10. Electrical conductivity of the two hosts tested before and after fusion with sulfur.

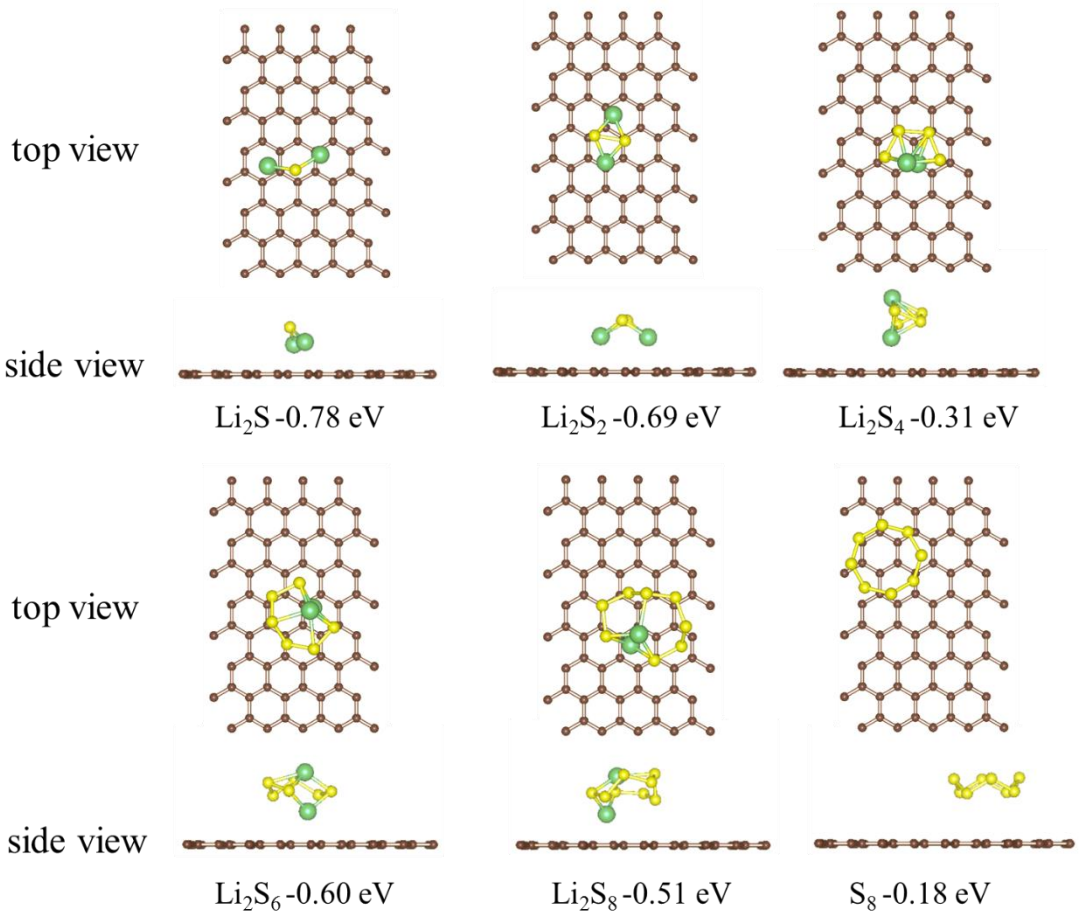

Figure S11. Binding energies and adsorbed structures of LiPS on the surface of carbon calculated by DFT.

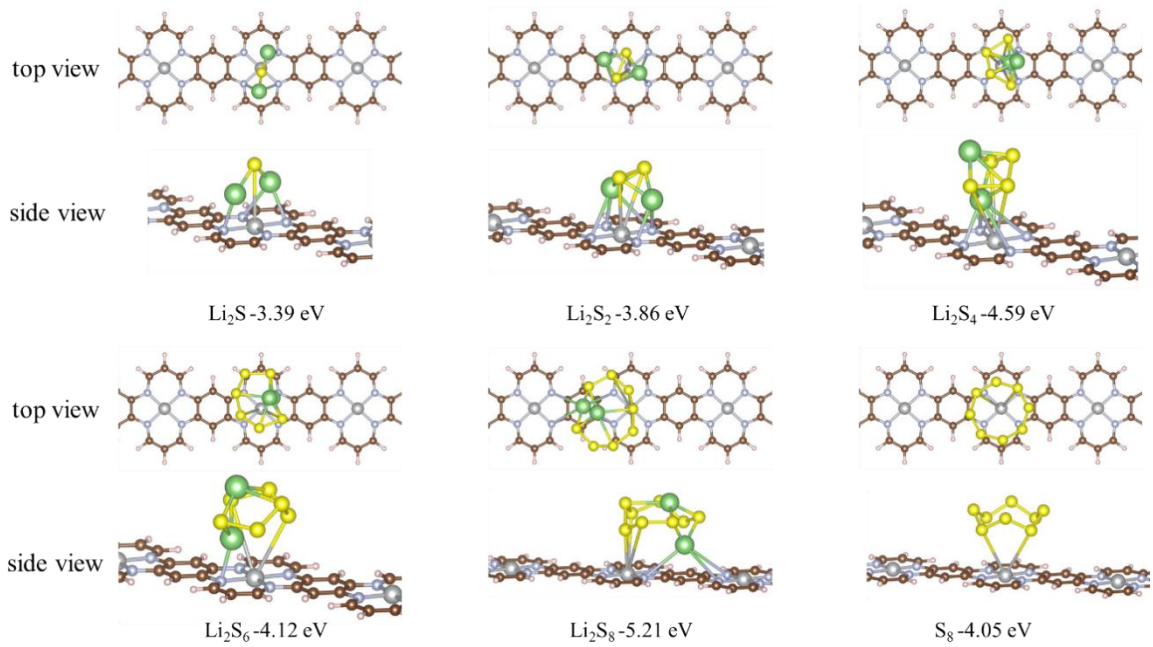

Figure S12. Binding energies and adsorbed structures of LiPS on the surface of Ni-MOF-1D calculated by DFT.

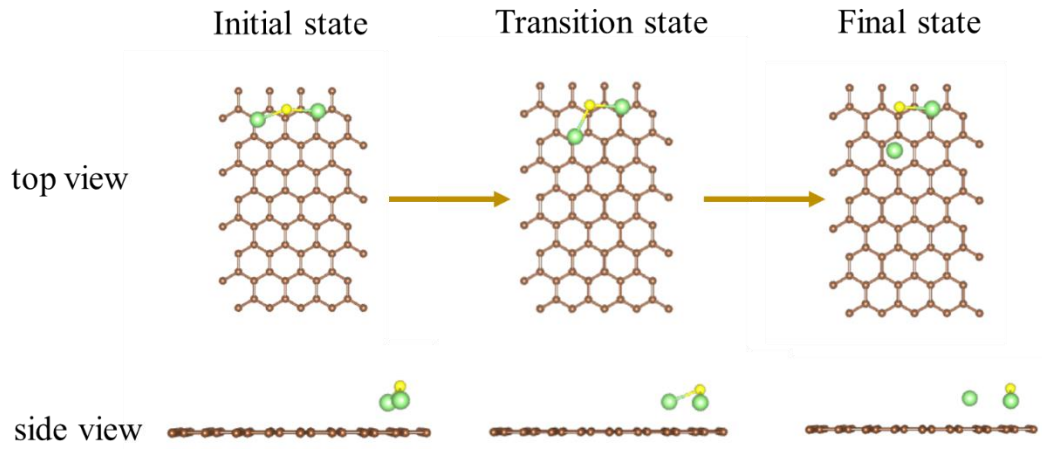

Figure S13. The optimized adsorption configuration of Li_2S decomposition on carbon.

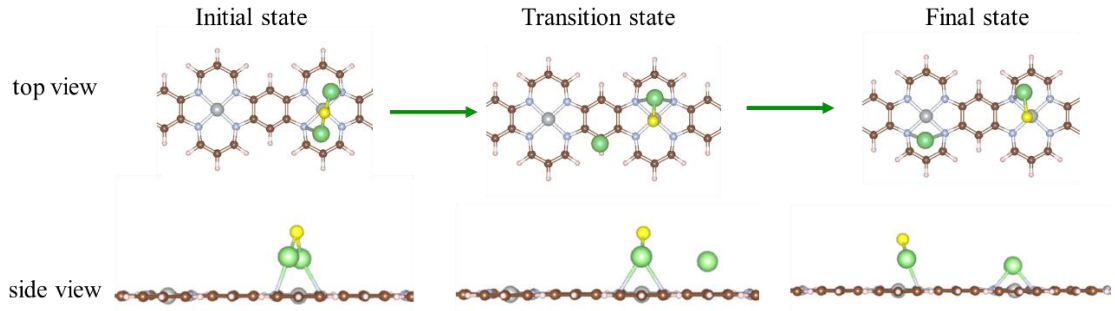

Figure S14. The optimized adsorption configuration of Li_2S decomposition on Ni-MOF-1D.

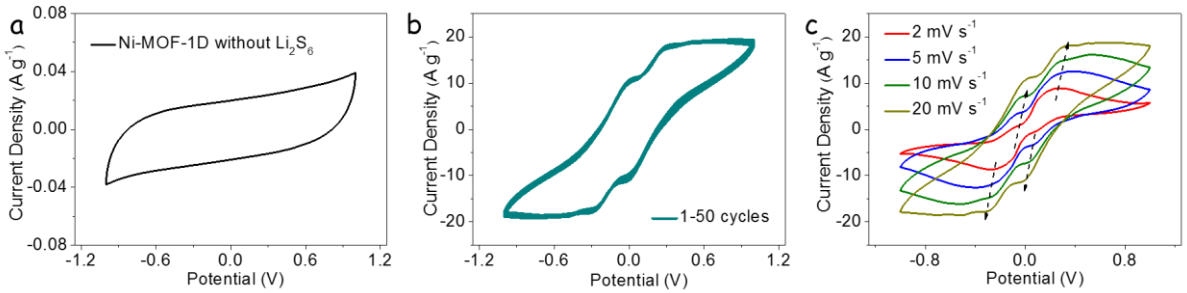

Figure S15. (a) CV curve of Ni-MOF-1D as electrode measured in symmetric coin cell configuration using an electrolyte containing 1 mol L^{-1} LiTFSI dissolved in DOL/DME (v/v = 1/1). (b) CV curves of symmetric cells from 1 to 50 cycles. (c) CV profiles of Ni-MOF-1D electrodes in symmetric cells at scan rate from 2 mV s^{-1} to 20 mV s^{-1}.

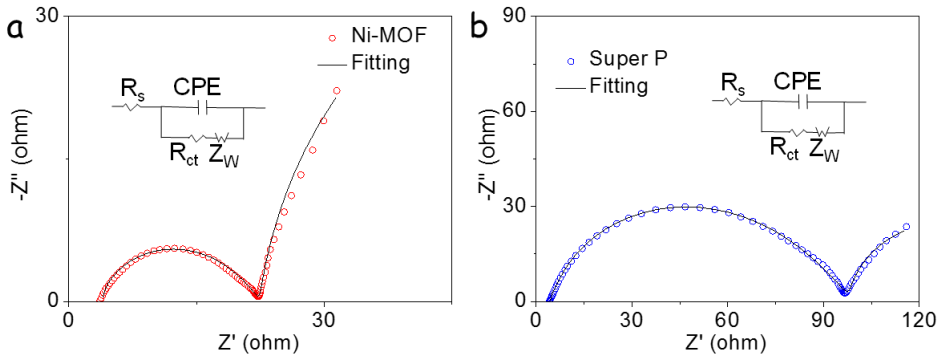

Figure S16. EIS spectra of symmetrical cells with different host materials, Ni-MOF-1D (a) and Super P (b), using an electrolyte containing 0.5 mol L^{-1} Li^2S^6 and 1 mol L^{-1} LiTFSI dissolved in DOL/DME (v/v = 1/1).

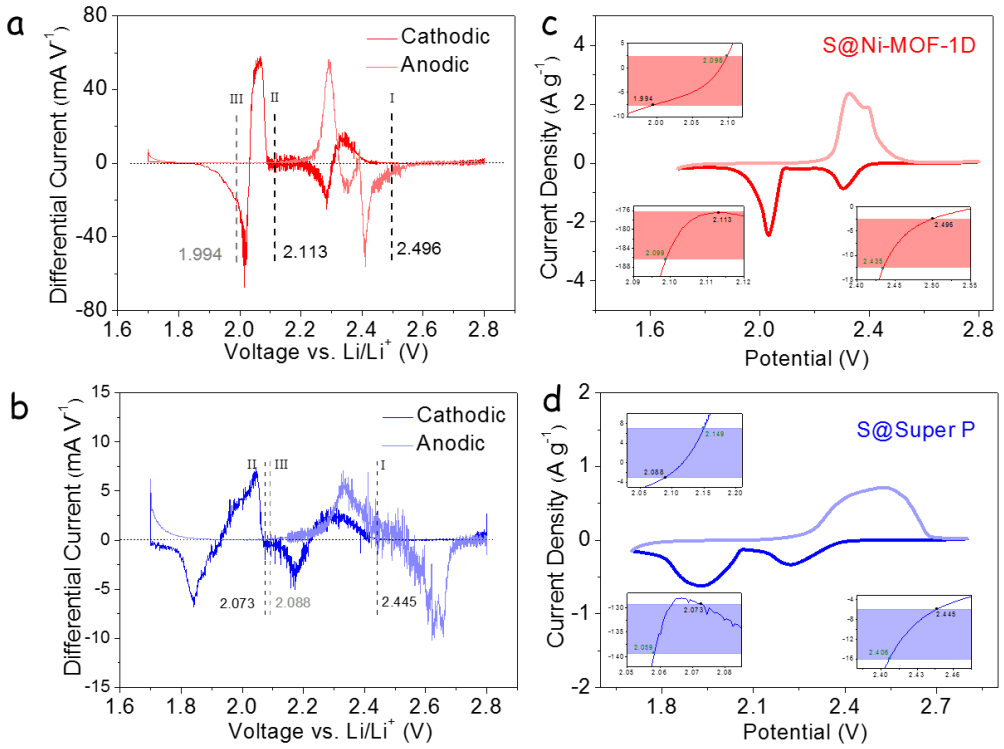

Figure S17. Onset potential for Li–S redox reactions. (a,b) Differential CV curves of S@Ni-MOF-1D (a) and S@Super P (b). The baseline voltage and current density are defined as the value before the redox peak, where the variation on current density is the smallest, namely dI/dV = 0. Baseline voltages are denoted in black for cathodic peak I, II, and in gray for anodic peak III, respectively. (c,d) CV curves and corresponding onset potentials of redox peak I, II, and III (inset): (c) S@Ni-MOF-1D, (d) S@Super P. Following a common definition employed in electrocatalysis, the onset potential is determined when the current density is 10 μA cm^{-2} beyond the corresponding baseline current density (more specifically, 10 μA cm^{-2} more negative than baseline current density for cathodic peaks or 10 μA cm^{-2} positive than baseline current density for anodic peaks). As shown in the inset of c and d, the baseline voltages are the same as in a and b, while the colored region indicates the gap in current density (10 μA cm^{-2}).

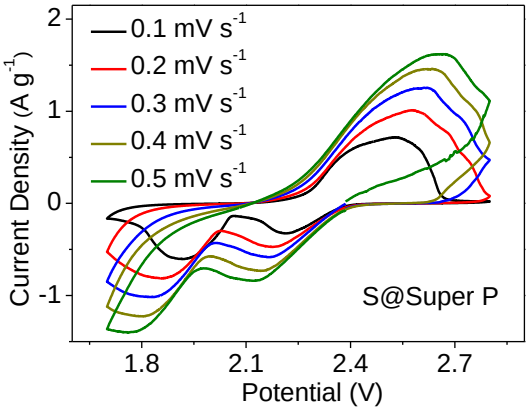

Figure S18. CV curves of S@Super P at different scan rates.

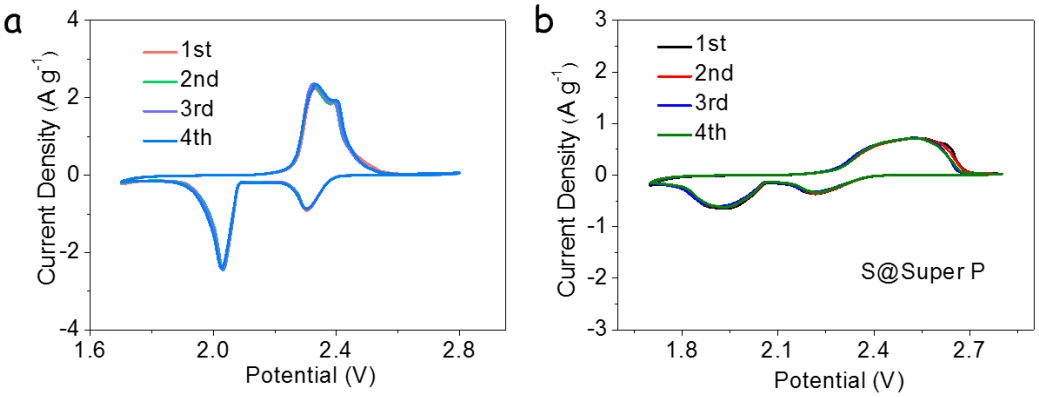

Figure S19. First four cycles of CV curves of (a) S@Ni-MOF-1D, and (b) S@Super P performed at a scan rate of 0.1 mV s^{-1}.

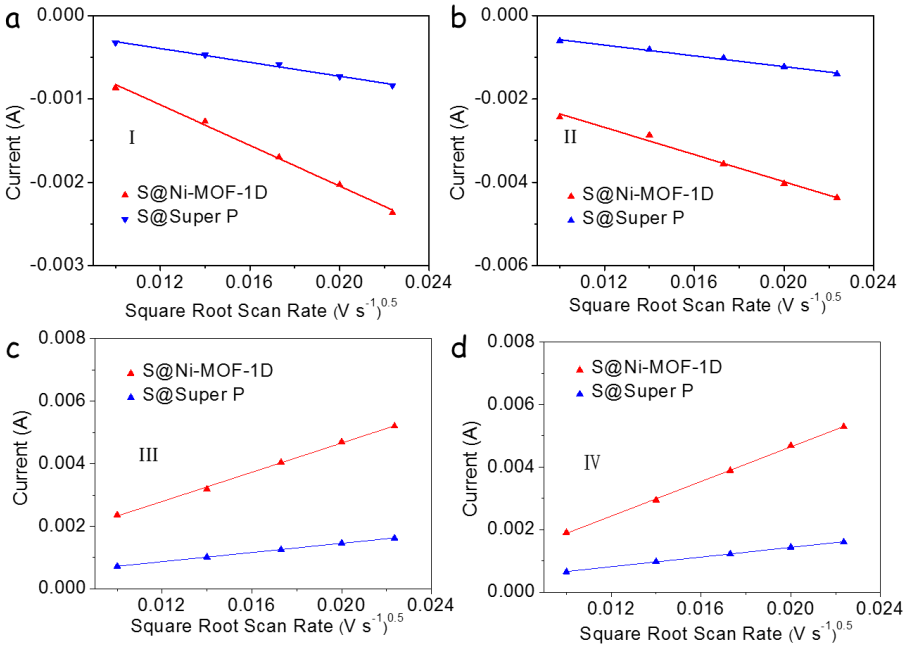

Figure S20. Plots of CV peak current for (a) the first cathodic reduction process (I: S_8 → Li_2S_4), (b) the second cathodic reduction process (II: Li_2S_4→ Li_2S_2/Li_2S), (c) the first anodic oxidation process (III: Li_2S_2/Li_2S →Li_2S_4), and (d) the second anodic oxidation process (IV: Li_2S_4→ S_8) versus the square root of the scan rates.

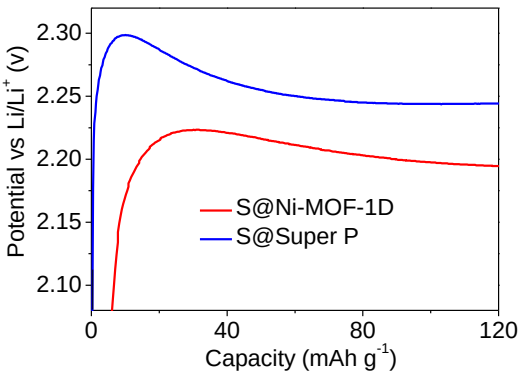

Figure S21. Charge profiles of S@Ni-MOF-1D, and S@Super P electrodes showing the overpotentials for conversion between soluble LiPS and insoluble Li_2S_2/Li_2S.

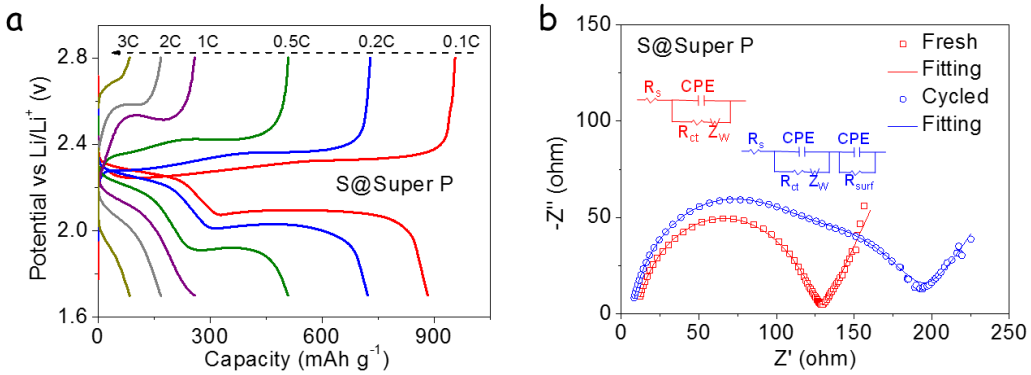

Figure S22. (a) Galvanostatic charge/discharge profiles of S@Super P electrodes at different current densities range from 0.1 C to 3 C. (b) EIS spectra of S@Super P coin cells before and after cycling. Blue trace corresponds to fresh cell and red trace to the same cell after cycling. The R_s, R_{ct}, R_{surf}, and Z_w stand for the resistance of the electrolyte, interfacial charge-transportation, insoluble Li_2S_2/Li_2S layer, and semi-infinite Warburg diffusion, respectively; and CPE stands for the corresponding capacitance.

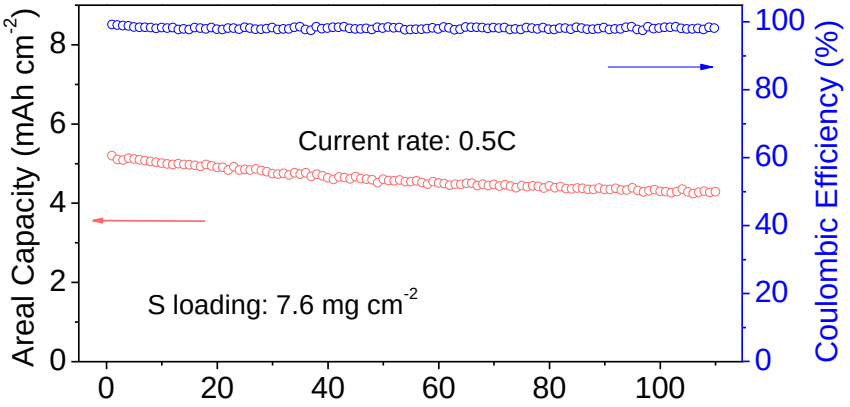

Figure S23. High-loading cycling performances with sulfur loadings of 7.6 mg cm^{-2} at 0.5 C of S@Ni-MOF-1D electrodes.

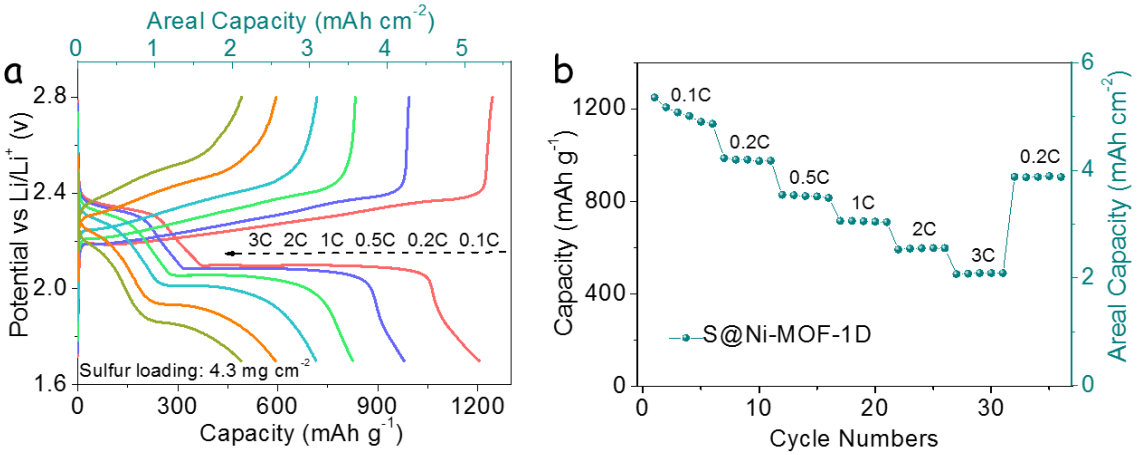

Figure S24. (a) Galvanostatic charge/discharge profiles of S@Ni-MOF-1D at various current rates with a high sulfur loading of 4.3 mg cm^{-2}. (b) Rate capability of S@Ni-MOF-1D cathodes loaded with 4.3 mg cm^{-2} of sulfur at various C rates.

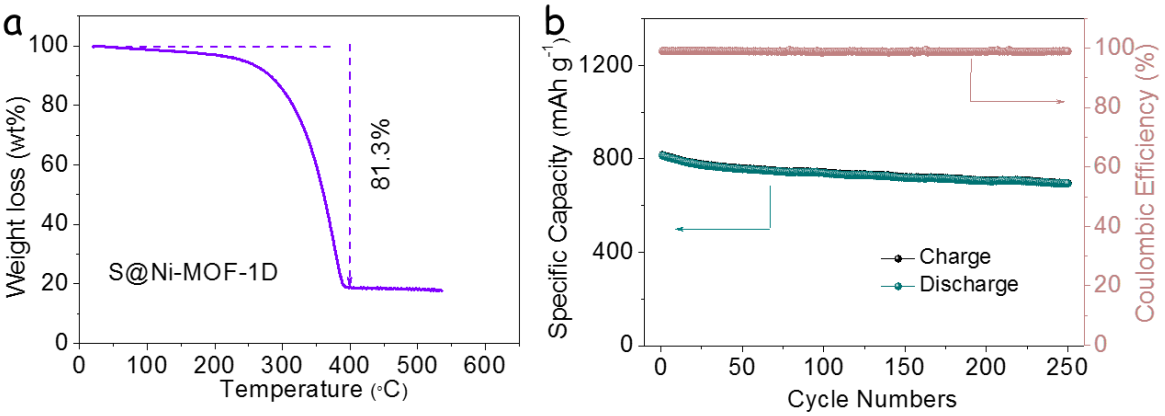

Figure S25. (a) TGA curve of a S@Ni-MOF-1D composite with a higher sulfur loading. (b) Cycling stability and Coulombic efficiency of the S@Ni-MOF-1D cathode with a higher sulfur loading at 1 C for 250 cycles.

Table S2 Summary of recent reports on MOF-based sulfur host cathodes for LSBs.

Host material	Capacity (mAh g^{-1}) (current rate)	(cycles, current rate)	Decay rate (per cycle, %)	S content (%)	Ref
Zr-MOF	1193 (0.1C)	(100, 0.2C)	0.29%	45%	6
DMAZF MOF	1260 (0.1C)	(120, 0.1C)	0.07%	70%	7
Cr-MOF	1190 (0.1C)	(300, 2.4C)	0.07%	41.2%	8
ZIF-8	1150 (0.2C)	(100, 0.1C)	0.085%	64%	9
HKUST-1	1102 (0.2C)	(500, 0.2C)	0.080%	40%	10
$Na_2Fe[Fe(CN)_6]$	1020 (0.1C)	(100, 0.1C)	0.251%	50%	11
MIL-53	1215 (0.1C)	(300, 0.5C)	0.186%	50%	12
Al/Cu-MOF	974.2 (0.1C)	(200, 0.1C)	0.25%	62%	13
RANEY® nickel	1469 (0.1C)	(500, 0.5C)	0.12%	36.6%	14
$Ni_3(HITP)_2$	1151 (0.2C)	(300, 1C)	0.116%%	65.5%	15
$Ni_6(BTB)_4(BP)_3$	689 (0.1C)	(100, 0.1C)	0.110%	60%	16
Ni-MOF-1D	**1491 (0.1C)**	**(1000, 3C)**	**0.018%**	**70.2%**	**This work**

References

[1] G. Kresse, J. Furthmüller, *Phys. Rev. B.* **1996**, *54*, 11169-11186.

[2] P. E. Blöchl, *Phys. Rev. B.* **1994**, *50*, 17953-17979.

[3] J. Sun, A. Ruzsinszky, J. P. Perdew, *Phys. Rev. Lett.* **2015**, *115*, 036402.

[4] J. Sun, R. C. Remsing, Y. Zhang, Z. Sun, A. Ruzsinszky, H. Peng, Z. Yang, A. Paul, U. Waghmare, X. Wu, M. L. Klein, J. P. Perdew, *Nat. Chem.* **2016**, *8*, 831-836.

[5] Q. Zhang, Y. Wang, Z. W. Seh, Z. Fu, R. Zhang, Y. Cui, *Nano Lett.* **2015**, *15*, 3780-3786.

[6] A. E. Baumann, X. Han, M. M. Butala, V. S. Thoi, *J. Am. Chem. Soc.* **2019**, *141*, 17891-17899.

[7] M. Rana, H. A. Al-Fayaad, B. Luo, T. Lin, L. Ran, J. K. Clegg, I. Gentle, R. Knibbe, *Nano Energy* **2020**, *75*, 105009.

[8] Z. Zhao, S. Wang, R. Liang, Z. Li, Z. Shi, G. Chen, *J. Mater. Chem. A.* **2014**, *2*, 13509-13512.

[9] H. Zhang, W. Zhao, M. Zou, Y. Wang, Y. Chen, L. Xu, H. Wu, A. Cao, *Adv. Energy Mater.* **2018**, *8*, 1800013.

[10] Y. Mao, G. Li, Y. Guo, Z. Li, C. Liang, X. Peng, Z. Lin, *Nat. Commun.* **2017**, *8*, 14628.

[11] D. Su, M. Cortie, H. Fan, G. Wang, *Adv. Mater.* **2017**, *29*, 1700587.

[12] J. Zhou, R. Li, X. Fan, Y. Chen, R. Han, W. Li, J. Zheng, B. Wang, X. Li, *Energy Environ. Sci.* **2014**, *7*, 2715.

[13] P. Geng, M. Du, X. Guo, H. Pang, Z. Tian, P. Braunstein, Q. Xu, *Energy Environ. Mater.* **2021**, DOI: 10.1002/eem2.12196.

[14] X. Zhu, J. Tian, X. Liu, W. Huang, D. Luo, Z. Wang, Z. Shan, *RSC Adv.* **2017**, *7*, 35482.

[15] D. Cai, M. Lu, Li, J. Cao, D. Chen, H. Tu, J. Li, W. Han, *Small* **2019**, *15*, e1902605.

[16] J. Zheng, J. Tian, D. Wu, M. Gu, W. Xu, C. Wang, F. Gao, M. H. Engelhard, J. G. Zhang, J. Liu, J. Xiao, *Nano letters.* **2014**, *14*, 2345-2352.